

1 **Constraints on the uptake of REE by scheelite in the**

2 **Baoshan tungsten skarn deposit, South China**

3 Wen Winston Zhao^a, Mei-Fu Zhou^{a,*}, Anthony E. Williams-Jones^{a,b}, Zheng Zhao^c

4 ^a *Department of Earth Sciences, The University of Hong Kong, Hong Kong, China*

5 ^b *Department of Earth and Planetary Sciences, McGill University, Montréal, Québec H3A 0E8, Canada*

6 ^c *Institute of Mineral Resources, Chinese Academy of Geological Sciences, Beijing 100037, China*

7

8

9

10

11

12

13

14

15

16

17

18

19 -----

20 ***Corresponding author:**

21 Prof. Mei-Fu Zhou

22 Email: mfzhou@hku.hk

23 Tel: +852-28578251

24 Fax: +852-25176912

25 ABSTRACT

26 Scheelite is the main ore mineral in skarn-type tungsten deposits, and a common
27 accessory mineral in a variety of rock-types. The Baoshan deposit in South China is
28 one of the most important polymetallic scheelite skarn deposits in China, hosting
29 40,000 t of WO₃ with economic concentrations of Zn, Cu, and Ag. It is hosted by a
30 calcic skarn that is zoned outwards mineralogically from garnet-clinopyroxene,
31 through clinopyroxene-garnet, to wollastonite, and overprinted by retrograde minerals.
32 Scheelite occurs in both the prograde and retrograde skarns, and is complexly zoned.
33 On the basis of its textures, the scheelite was classified into three types. Scheelite I
34 and II belong to the early and late prograde stages, respectively, and Scheelite III
35 precipitated during the retrograde stage. The molybdenum (Mo) content of these
36 scheelite types ranges from 54 ppm to 24 wt.%, and the total rare earth element
37 content ranges from 12 to 321 ppm. Rare earth element (REE) concentrations and
38 chondrite-normalized REE profiles vary with the distribution of major elements. The
39 profiles indicate variable degrees of REE enrichment, which correlates negatively
40 with the Mo content. Molybdenum-rich scheelite displays a negative Eu anomaly, and
41 Mo-poor scheelite a positive Eu anomaly. Crystal structure provided the first-order
42 control on the minor and trace element composition of the scheelite. Incorporation of
43 REE³⁺ into scheelite was controlled partly by a coupled substitution involving Mo.
44 The lattice strain model was used to estimate scheelite-fluid partition coefficients for
45 the REE from the contents of these elements in the scheelite and to predict the relative
46 distributions of the REE in the ore-forming fluids. It is proposed that conditions were
47 initially oxidizing, leading to strong incorporation of Mo in Scheelite I, that they
48 became more reducing with the crystallization of Scheelite II containing lesser Mo,
49 and that during retrograde skarn formation there was a return to oxidizing conditions

50 due to an influx of meteoric waters, which altered Scheelite II giving rise to the
51 formation of Scheelite III. The study shows that the composition of scheelite recorded
52 the history of the Baoshan hydrothermal system, and that the behaviour of the REE
53 could be used to quantitatively reconstruct the changing physicochemical conditions
54 during ore formation.

55 **Keywords:** Skarn deposit; Scheelite; Rare earth elements; Lattice Strain Model; South
56 China

57

58 1. Introduction

59 Rare earth elements (REEs) are important as geochemical tracers ([Lipin et al.,](#)
60 [1989](#); [Linnen et al., 2014](#)). They are widely used in petrogenetic studies of magmatic
61 systems because the distribution of the REE in in the bulk rock and minerals varies
62 with the magmatic process, e.g., magma mixing, magmatic assimilation and fractional
63 crystallization, as well as with the source of the magma ([Hanson, 1980](#)). The controls
64 on the partitioning of the REE between melt and minerals are relatively well
65 understood. Little is known, however, about the partitioning of the REE between
66 minerals and hydrothermal fluids, and consequently there have been few studies
67 employing REE as geochemical tracers in hydrothermal systems (e.g., [Bau, 1996](#);
68 [Ghaderi et al., 1999](#); [Brugger et al., 2000](#); [Smith et al., 2004](#); [Brugger et al., 2008](#);
69 [Gaspar et al., 2008](#)).

70 Many studies have shown that, in hydrothermal systems, adjacent isovalent REEs
71 can be fractionated from one another depending on the crystal structure and the
72 chemistry of the fluids (e.g., [Bau, 1991](#); [Williams-Jones et al., 2012](#); [Migdisov and](#)
73 [Williams-Jones, 2014](#); [Migdisov et al., 2016](#)). Thus, in principle, the serial behaviour
74 of the REE should allow them to become powerful tools for interpreting hydrothermal
75 processes (e.g., [Smith et al., 2004](#); [Gaspar et al., 2008](#)), although the capacity of the
76 REE to complex with multiple ligands may complicate this application ([van Hinsberg](#)
77 [et al., 2010](#)). Until now, applications of inter-element fractionation among the REEs
78 in hydrothermal systems have largely been limited to geochronologic and other types
79 of isotopic studies, particularly those involving fractionation between Sm and Nd
80 (e.g., [Poitrasson et al., 1998](#); [Brugger et al., 2002](#); [Smith et al., 2004](#)). Significantly,
81 only two studies have employed a full set of REE to interpret hydrothermal systems,
82 namely those of [Ghaderi et. al. \(1999\)](#) and [Brugger et al. \(2000\)](#), who used the REE

83 chemistry of scheelite to gain insights into fluid evolution in orogenic gold ore-
84 depositing systems.

85 Scheelite is a common mineral in skarn, porphyry, hydrothermal vein, and
86 metamorphic stratabound deposits (e.g., [Brugger et al., 1998](#); [Uspensky et al., 1998](#);
87 [Brugger et al., 2000](#); [Song et al., 2014](#); [Guo et al., 2016](#)). It has a simple crystal
88 structure with tetrahedral $[\text{WO}_4]^{2-}$ groups and irregular dodecahedral $[\text{CaO}_8]^{14-}$ groups,
89 and a basic formula of CaWO_4 with tetragonal symmetry. The Mo^{6+} ion can substitute
90 for W^{6+} in any proportion to form a complete solid solution between scheelite
91 (CaWO_4) and powellite (CaMoO_4) ([Hsu and Galli, 1973](#); [Tyson et al., 1988](#)). Owing
92 to ionic radii that are similar to that of Ca, significant amounts of REEs, Sr, Nb, and
93 Pb can also substitute into the scheelite structure ([Raimbault et al., 1993](#)).

94 In this paper, we describe the petrography of scheelite from the Baoshan
95 polymetallic tungsten skarn deposit of South China, and present results of *in situ*
96 major and trace element analyses for this mineral. The purpose of this study is to
97 decipher scheelite chemistry in this deposit, and to determine how the evolving
98 distribution of the REE in relation to Mo and Nb in this mineral might be used to gain
99 a better understanding of hydrothermal ore-forming processes at Baoshan and
100 elsewhere.

101 2. Geological Setting

102 The Baoshan skarn deposit is located in the town of Qianchang, about 50 km
103 southwest of Ganzhou City, South China ([Fig. 1](#)). Although sulfide ores (e.g.,
104 sphalerite, chalcopyrite, and pyrrhotite) have been mined at Baoshan since the Ming
105 Dynasty (17th century BCE), and slags dating to this time have been discovered in the
106 Western Ore Zone, it was not until 1967, that the Geological Team of Jiangxi
107 Province recognized its tungsten mining potential, and carried out the first modern

108 exploration. The deposit contains about 40,000 t of WO₃ grading ~0.5 wt%,
109 accompanied by economic concentrations of Zn, Cu, and Ag, making it one of the
110 most important polymetallic tungsten skarns in China ([Zhao et al., 2017](#)).

111 The tungsten skarns are located along the contacts between the Mesozoic
112 Baoshan granitic pluton and the Carboniferous Huanglong and Chuanshan Formations
113 ([Fig. 1](#)). The latter are composed mainly of limestone, which is accompanied by
114 minor dolomitic limestone, and sandwiched between sandstone and siltstone of the
115 Lower Carboniferous Zishan Formation and Permian Maokou Formation. The
116 Baoshan granitic pluton comprises equigranular and porphyritic facies and has a S-
117 type composition ([Guo, 2010](#)). It was emplaced at ~160 Ma during crustal extension
118 associated with the subduction of the paleo-Pacific plate ([Zhou et al., 2006](#); [Guo,](#)
119 [2010](#); [Mao et al., 2013](#); [Zhao and Zhou, 2015](#); [Zhao et al., 2017](#)). The most important
120 fault in the area, the northeastern-trending Tongtianyan strike-slip Fault, displaced the
121 Carboniferous and Permian strata and the Mesozoic granites ([Fig. 1](#)).

122 The deposit has been subdivided into four ore zones: the Western Ore Zone,
123 Northern Ore Zone, Eastern Ore Zone, and Southern Ore Zone. The most important of
124 these zones, the Eastern Ore Zone, is currently the main mining site ([Fig. 1](#)).
125 Tungsten-mineralized skarns are best developed in this ore zone, and are distributed,
126 both horizontally and vertically, in zones where the contacts between the granites and
127 marble define embayments in the granites; they are most weakly developed where the
128 contacts define salients ([Fig. 1](#)). Skarns in the embayments are usually several meters
129 in width ([Fig. 2A](#)). They are dominated by anhydrous prograde mineral assemblages,
130 and are zoned outwards mineralogically from coarse-grained grandite garnet adjacent
131 to the granite, through grandite garnet-calcic clinopyroxene and fine-grained calcic
132 clinopyroxene, to minor wollastonite (±vesuvianite) adjacent to marble ([Fig. 2B](#)).

133 Minor subcalcic garnet with magnetite occurs in the endoskarns, which are of very
134 limited extent. Retrograde skarn assemblages, including the hydrous silicates,
135 ferroactinolite, epidote, and chlorite, and the sulfides, chalcopyrite, pyrrhotite,
136 sphalerite, and molybdenite, replaced the margins of the prograde skarn minerals, and
137 occur in interstices among these minerals and in veins.

138 **3. Methodology**

139 This study was based on 10 samples of pyroxene skarn rich in scheelite that were
140 collected on underground Level 410 of the Baoshan deposit (Fig. 1). These samples
141 were coarsely crushed and the scheelite rich fragments were mounted in epoxy
142 holders (BSS5-1, BSS5-2, BSS5-3, BSS5-4, BSS5-6, and BSS5-7) and polished for
143 microscopic observation and analysis.

144 Scheelite was identified in mounts and sections using a Leica DM RD polarizing
145 microscope at the Department of Earth Sciences, The University of Hong Kong
146 (HKU). Selected samples were observed using a Hitachi S-3400N scanning electron
147 microscope (SEM) under high vacuum (10^{-5} torr) and in variable pressure mode (10^{-1}
148 torr) at the Electronic Microscopy Unit, HKU. Semiquantitative analyses of scheelite
149 were conducted using an energy dispersive X-ray analysis system (EDS) with an
150 accelerating voltage of 15 kV, a working distance of 10 mm, and Thermo Scientific
151 NORAN System SIX software. Backscatter electron (BSE) imaging was performed
152 using a high-sensitivity semiconductor detector located directly above the sample.
153 Cathodoluminescence imaging (CL) was performed at the State Key Laboratory of
154 Continental Tectonics and Dynamics, Chinese Academy of Geological Sciences,
155 using a Cathode generator Mono CL4 detector, operated at about 15 kV and 20 nA.

156 Electron Microprobe (EMP) analyses were carried out at the Department of Earth
157 Sciences, HKU. Major element compositions of scheelite, clinopyroxene, and garnet

158 were obtained by wavelength dispersive spectrometry using a JEOL JXA8230
159 electron microprobe operating at an accelerating voltage of 20 kV with a 20 nA beam
160 current, 1 μm beam diameter, and a 10-30 s counting time. The precision of all
161 analyzed elements was better than 1.5%. Minerals and synthetic oxides were used as
162 standards. All data were corrected using the ZAF procedure.

163 Trace element contents of scheelite and clinopyroxene were measured by Laser
164 Ablation Inductively Coupled Plasma Mass Spectroscopy (LA-ICP-MS) at the
165 FocuMS Mass Spectroscopy Laboratory, Nanjing. Laser sampling was performed
166 using a Photon Machines Excite 193nm laser ablation system, coupled to an Agilent
167 7700x ICP-MS with a 1 m transfer tube. Helium was used as a carrier gas and argon
168 was used as the make-up gas and mixed with the carrier gas via a T-connector before
169 entering the ICP. The carrier and make-up gas flows were optimized by ablating the
170 NIST SRM 610 standard to obtain maximum signal intensity while keeping low
171 ThO/Th (0.1-0.3%) and $\text{Ca}^{2+}/\text{Ca}^{+}$ (0.4-0.7%) ratios to reduce the oxide and doubly
172 charged ion interferences. The $^{238}\text{U}/^{232}\text{Th}$ ratio, which was used as an indicator of
173 complete vaporization, was kept at ~ 1 while ablating NIST SRM 610. Each analysis
174 incorporated ~ 30 s of background acquisition (gas blank) followed by 50 s of data
175 acquisition from the sample. A spot with a diameter of 25 μm was used to ablate
176 zones in scheelite crystals, whereas a spot with a diameter of 70 μm was used to
177 ablate domains in clinopyroxene crystals. Every eighth to tenth spot analysis was
178 followed by a NIST SRM 610 analysis to correct the time-dependent drift of
179 sensitivity and mass discrimination of the ICP-MS ([Liu et al., 2008](#); [Sun and Chen,](#)
180 [2017](#)). Reference glasses (GSE-1G, BHVO-2G, BCR-2G, and NIST SRM 612) were
181 analyzed prior to and after the sample measurements. The NIST SRM 610 glass was
182 used as an external calibration standard, and the Ca content of each scheelite crystal

183 and Si of each clinopyroxene crystal, which had been analyzed using the electron
184 microprobe were used as internal standards. Off-line selection and integration of
185 background and analyte signals, and time-drift correction and quantitative calibration
186 were performed by ICPMSDataCal ([Liu et al., 2008](#); [Liu et al., 2010](#)). The precision
187 and accuracy were within 10% of the reported values; for values used in the lattice
188 strain calculations they were within 5%.

189 4. Skarn Mineralogy

190 Based on the observed textural relationships, the mineral paragenesis in the
191 Baoshan scheelite skarn was subdivided into two main stages ([Fig. 3](#)), a high-
192 temperature prograde skarn stage and a low-temperature retrograde skarn stage. The
193 earliest prograde skarns are characterized by Mg-enriched clinopyroxene ($\text{Di}_{62-41}\text{Hd}_{43-}$
194 $_{28}\text{Jo}_{17-11}$), and Al-enriched garnet ($\text{Grs}_{76-60}\text{And}_{14-11}\text{Sps}_{30-11}$); there is a zone of
195 wollastonite in contact with the marble ([Fig. 4A](#)). Minor Mo-enriched scheelite occurs
196 together with Mg-rich clinopyroxene as inclusions in early Al-rich garnet ([Fig. 4B](#)).
197 The early Mg-rich clinopyroxene and Al-rich garnet were replaced and rimmed by
198 late Fe-rich clinopyroxene ($\text{Di}_{11-4}\text{Hd}_{87-81}\text{Jo}_{16-11}$) ([Fig. 4C](#)) and Fe-rich garnet (Grs_{30-}
199 $_{2}\text{And}_{95-67}\text{Sps}_{4-3}$) ([Fig. 4D-E](#)), respectively, and accompanied by fluorite ([Fig. 4E](#)),
200 which formed during the late prograde skarn mineral stage.

201 The retrograde stage overprints the prograde stage mineral assemblages. Prograde
202 minerals, such as garnet, were transformed into hydrous minerals (e.g., epidote) and
203 subsequently carbonate ([Fig. 4E-F](#)). However, an Al-rich garnet ($\text{Grs}_{66-40}\text{And}_{20-}$
204 $_{15}\text{Sps}_{39-17}$) was also deposited; it occurs in millimeter- to centimeter-wide discordant
205 veins that cut the prograde skarn ([Fig. 4H](#)). Newly formed hydrous minerals (e.g.,
206 chlorite) and carbonate also precipitated in the pores of early minerals ([Fig. 4g](#)).
207 During the late retrograde stage, sulfides precipitated around the early retrograde

208 minerals or in centimeter- and/or meter-thick bands along fractures and lithologic
209 contacts (Fig. 4H). The most abundant sulfide is pyrrhotite, although molybdenite,
210 chalcopyrite, sphalerite, galena, and native bismuth also have been identified..

211 The late prograde hedenbergite skarn, which contains a high proportion of
212 scheelite, is the main skarn type at Baoshan. The scheelite in this skarn occurs either
213 as inclusions in the clinopyroxene (Fig. 5A) or as small subrounded isolated
214 disseminated crystals that are frequently intergrown with the clinopyroxene (Fig. 5B).
215 In back-scattered electron images (BSE), isolated scheelite crystals exhibit texturally
216 complex zoning patterns as dark and light domains (Fig. 6A), with the cores being
217 richer in Mo than the rims. The light domains form vein-like structures that, together
218 with molybdenite, crosscut the dark domains. Locally, they also form breccias that
219 cement fragments of the dark domains. The dark inner domains represent primary
220 Scheelite I, whereas the light domains clearly formed later and could represent the
221 late prograde stage (Scheelite II) or the retrograde stage (Scheelite III). In the
222 corresponding cathodoluminescence (CL) image (Fig. 6B), the light domains display
223 contrasting lighter and darker domains. Moreover, the darker domains, which show
224 evidence of oscillatory zoning, in some cases, are surrounded or crosscut by lighter
225 domains (Fig. 6C), and locally fluorite (white) is enclosed by the lighter domains (Fig.
226 6D). These relationships indicate that the oscillatory-zoned (darker) scheelite is
227 Scheelite II, that it precipitated together with fluorite and that the lighter scheelite,
228 which mostly co-exists with molybdenite (Fig. 6E), is Scheelite III. The scheelite
229 filling interstices among clinopyroxene crystals (Fig. 5A) is light in BSE images (Fig.
230 6F), and in CL images consists mainly of light domains surrounding dark domains
231 (Fig. 6G). This scheelite is therefore interpreted to be Scheelite II (CL-dark) that was
232 overprinted by Scheelite III (CL-light).

233

234 5. Scheelite chemistry

235 Compositional data for scheelite from the Baoshan skarn deposit are presented in
236 Table 1 and Supplementary Data Table A1. As might be expected from the BSE and
237 CL imaging, this scheelite varies considerably in composition. The concentrations of
238 the major element oxides, WO_3 and CaO , range from 54.91 to 82.17 wt%, and from
239 19.39 to 22.28 wt%, respectively. Molybdenum is both a major and a trace element,
240 ranging from a concentration high of 24.12 wt% MoO_3 to a low of 54 ppm Mo. Taken
241 together, the contents of these three element oxides reflect the fact that the scheelite is
242 actually a scheelite-powellite solid solution ranging compositionally from end-
243 member scheelite to a variety containing 41% of the powellite component.

244 The only elements, in addition to those mentioned above, that are in significant
245 concentration in the scheelite, are Na (below detection to 50 ppm), Sr (16 to 72 ppm),
246 Nb (3 to 122 ppm), Ta (below detection to 0.5 ppm), Pb (2 to 8 ppm), and the REEs
247 (12 to 321 ppm). Concentrations of Zr and Hf are below the detection limits of LA-
248 ICP-MS (<0.1 ppm). Normalized to chondrite, the scheelite is enriched in light REEs
249 (LREEs), depleted in middle and heavy REEs (MREEs and HREEs) and displays
250 both negative and positive Eu anomalies (Fig. 7).

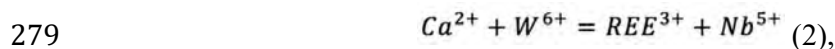
251 Scheelite I has a very high Mo content (56,000 to 160,000 ppm) and relatively
252 low ΣREE content (12 to 158 ppm), with MREE and HREE contents being mostly
253 below the detection limit (Fig. 8A). Two subgroups can be distinguished on the basis
254 of their Mo and REE contents. Scheelite Ia has the higher Mo content and a low
255 ΣREE content, whereas Scheelite Ib (lower Mo content) contains a much higher
256 ΣREE concentration (Fig. 9). Both Scheelite Ia and Ib exhibit small negative
257 chondrite-normalized Eu anomalies. Scheelite II has an intermediate Mo content

(6,900 to 9,900 ppm) and a content of ΣREE , which is generally greater than that of Scheelite I (114 to 197 ppm). Concentrations of the MREEs are higher than those of Scheelite I, but most of the HREEs have concentrations below the detection limit and, as for Scheelite I, there is a small negative Eu anomaly (Fig. 8B). Scheelite III has the lowest Mo content of the three scheelite types (54 to 90 ppm), but a wide range of ΣREE content, from 42 to 321 ppm. In contrast to Scheelite II, the concentrations of even the HREEs are above the detection limit, and there is a strong positive Eu anomaly (Fig. 8C). Moreover, the Eu anomalies of Scheelite I and Scheelite II are similar (negative) with a 1:1 slope below the $\text{Eu}_\text{N}/\text{Eu}_\text{N}^*=1$ line, whereas those of Scheelite III (positive) are variable above the $\text{Eu}_\text{N}/\text{Eu}_\text{N}^*=1$ line (Fig. 10A). However, the Eu anomalies of the three types of scheelite do not show any obvious correlation with Mo content, except for the two Scheelite III crystals with smaller positive Eu anomalies that have higher Mo contents than the crystal with the large positive Eu anomaly (Fig. 10B).

6. Discussion

6.1. Substitution of REEs for Ca in scheelite

The substitution of REE^{3+} for Ca^{2+} requires a charge-compensating mechanism to maintain electrical neutrality (McIntire, 1963). Several coupled substitution mechanisms involving REE^{3+} and Ca^{2+} in both the eightfold and fourfold coordination sites have been proposed (e.g., Nassau and Loiacono, 1963; Burt, 1989):

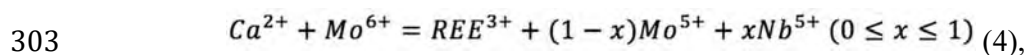


and



where $\square\text{Ca}$ represents the Ca-site vacancy.

It is possible to assess the relative importance of the different substitutions using binary plots of the concentrations of the substituting and substituted elements (e.g., Ghaderi et al., 1999; Brugger et al., 2000; Song et al., 2014). The low concentration of Na and poor correlations between Na and REE (Fig. 11A) indicate that the eightfold-site Na compensation mechanism (Substitution 1) did not play an important role in the incorporation of the REEs into the scheelite. On the other hand, the concentration of Nb is elevated (Table 1), and binary plots display generally positive correlations of Nb+Ta and $\Sigma\text{REE-Eu+Y}$ concentrations for Scheelite Ib and II (Fig. 11B), implying that a substitution involving Nb could have been important for these varieties of scheelite. However, the slopes for the most Mo-enriched Scheelite Ia and most Mo-depleted Scheelite III approach zero, unexpectedly indicating that substitution of the REE was not coupled significantly to that of Nb. It should be noted that the most Mo-depleted Scheelite III has higher contents of Nb and REEs than the most Mo-enriched Scheelite Ia, and that Mo-poor Scheelite Ib and Scheelite II is relatively enriched in Nb (Table 1), implying that Mo in scheelite has a negative effect on the incorporation of Nb. Considering that the radius of Nb^{5+} (0.48 Å) is closer to that of Mo^{5+} (0.46 Å) than those of Mo^{6+} (0.41 Å) and W^{6+} (0.42 Å) (Shannon, 1976), the incorporation of Nb could have been coupled mainly to the concentration of Mo^{5+} in the corresponding scheelite, and thus the incorporation of the REE was likely due to:



where x is a variable that depends on how much Nb^{5+} can substitute for Mo^{5+} in the fourfold site. This reaction shows that a lower $\text{Mo}^{6+}/\text{Mo}^{5+}(\text{Mo}^{4+})$ ratio (e.g., Scheelite II) would favour the incorporation of the REEs more than a higher ratio (e.g., Scheelite Ia). Furthermore, only Mo^{5+} (0.46 Å) can replace W^{6+} (0.42 Å) or Mo^{6+}

(0.41 Å), and Mo⁴⁺ does not substitute in the fourfold coordination site (Shannon, 1976). This implies that during the later Mo-depleted Scheelite III period, Mo⁴⁺ was dominant in the system consistent with the occurrence of molybdenite.

6.2. Modeling REE partitioning

6.2.1. The Lattice Strain Model

The distribution of a trace element between a mineral and a liquid (melt or aqueous fluid) can be described by a partition coefficient that is under the first-order control of the properties of a major element site in the mineral. Accordingly, the partitioning of isovalent cations can be explained by a simple model involving the size and elasticity of the crystal lattice sites (Blundy and Wood, 2003). The quantitative relationship between the elastic properties of a crystal and its element partitioning is referred to as the lattice strain model (LSM) (Brice, 1975; Blundy and Wood, 1994).

In the LSM, the partition coefficient D_i at equilibrium for a cation with radius r_i entering a particular crystal lattice site, M, is given by:

$$D_i = D_0 \exp \left\{ \frac{-4\pi E_M N_A}{RT} \cdot \left[\frac{r_0 (r_i - r_0)^2}{2} + \frac{(r_i - r_0)^3}{3} \right] \right\} \quad (5),$$

where D_0 is the partition coefficient of an isovalent ion of radius r_0 , which enters the site without strain, E_M is the Young's modulus of site M, N_A is Avogadro's Number, R is the universal gas constant, and T is temperature in Kelvin. The relationship is most often illustrated on an Onuma diagram as the logarithm of the partition coefficient versus the ionic radius (Fig. 12A):

$$\log D_i = \log D_0 - \frac{4\pi N_A \log e}{R} \cdot \frac{E_M}{T} \cdot \left[\frac{r_0 (r_i - r_0)^2}{2} + \frac{(r_i - r_0)^3}{3} \right] \quad (6),$$

330 which produces a parabolic distribution. The value for D_0 for a cation with optimal
331 radius, r_0 , fixes the “height” of the parabola, the curvature of which is controlled by T
332 and E for the site M. The parameters, r_0 , E , and T establish the deviations of the
333 partition coefficients from D_0 , and when combined with D_0 , yield the partition
334 coefficients, D_i (e.g., those for a series of cations, such as the REEs).

335 The first step in applying the LSM is to determine the values of D_0 , r_0 , and E . In
336 the case of the partitioning of elements between a mineral and a melt, the best
337 approach to calculating these parameters involves fitting the partitioning data for
338 experimental or natural mineral-glass pairs (e.g., [Hill et al., 2011](#)). It is also possible
339 to estimate the r_0 and E values of any mineral from the empirical equations of [Hazen](#)
340 [and Finger \(1979\)](#). However, it is not possible to reliably estimate D_0 without
341 information on the composition of the mineral and coexisting glass (or in our case
342 aqueous fluid), and the pressure-temperature conditions. Unfortunately, neither
343 mineral-aqueous liquid or mineral-melt partitioning data are available for scheelite,
344 and thus it is not possible to reliably calculate absolute partition coefficients for this
345 mineral with aqueous liquid. On the other hand, as D_0 only determines the “height” of
346 the parabola, it should be possible, in principle, to determine the relative values or
347 ratios of the partition coefficients for a given set of elements of the same charge, in
348 the case of this study, the REE.

349 6.2.2. Determining LSM parameters for Scheelite II

350 Rather than evaluating the partition coefficients for scheelite directly from r_0 and
351 E values determined using the equations in [Hazen and Finger \(1979\)](#), and selecting an
352 arbitrary value of D_0 , we decided to approach the problem indirectly. This approach
353 involved evaluating the partition coefficients for Fe-rich clinopyroxene (which was
354 roughly coeval with Scheelite II) from the values of the corresponding mineral-melt

355 LSM parameters, and using them and the clinopyroxene REE chemistry to calculate
356 the concentrations of the REE in the Baoshan fluid. We then employed these latter
357 concentrations to regress values of the LSM parameters for scheelite. The advantage
358 of this approach is that it afforded us an opportunity to test the reliability of our
359 relative REE concentrations by comparing the calculated r_0 and E values for scheelite,
360 with those computed using the equations of [Hazen and Finger \(1979\)](#).

361 The values of D_0 , r_0 and E for clinopyroxene employed in the calculations were
362 taken from [Olin and Wolff \(2010\)](#), who determined partition coefficients for REEs
363 between clinopyroxene and melt in natural samples (coexisting clinopyroxene and
364 volcanic glass) that are compositionally very similar to the clinopyroxene of the
365 Baoshan skarn, i.e., dominated by Ca in the eightfold site and Fe^{2+} in the sixfold site
366 ([Supplementary Data Table A2](#)). They extracted values of r_0 , E and D_0 by fitting their
367 data to a two-site (sixfold and eightfold co-ordination) LSM and obtained sets of
368 values for r_0 , E and D_0 for each site. To minimize the effect of temperature, we
369 selected the values of these parameters for their lowest temperature sample (namely
370 the Bandolier Tuff), which was emplaced at 700 °C, i.e., close to the probable
371 temperature of the granitoid magma and exsolving magmatic hydrothermal fluid that
372 was responsible for prograde skarn formation at Baoshan. Using these values
373 ($r_0=1.055$ Å, $E=3,390$ kbar, and $D_0=9.0$ for the eightfold site; $r_0=0.772$ Å, $E=11,000$
374 kbar, and $D_0=200$ for the sixfold site), we calculated the clinopyroxene-fluid REE
375 partition coefficients ([Fig. 12B](#)), and based on them and the contents of the REEs in
376 the Baoshan Fe-rich clinopyroxene, we estimated the concentrations of the REEs in
377 the hydrothermal fluid that would have been in equilibrium with this Fe-rich
378 clinopyroxene.

379 As illustrated in [Figure 12C](#), the Baoshan fluid is predicted to have had a
380 chondrite-normalized REE profile characterized by strong enrichment in the LREE,
381 depletion in the MREE and modest enrichment in the HREE. Significantly, the profile
382 is very similar in shape to that reported by [Banks et al. \(1994\)](#) for magmatic
383 hydrothermal fluids from the Capitan Mountains, New Mexico, USA, which, to our
384 knowledge represents the only comprehensive study of the REE content of fluids
385 from a granitoid-related magmatic hydrothermal system. Their profiles for the fluid
386 prior to saturation with REE minerals display very strong enrichment in the LREE
387 and flattening towards the HREE, whereas for the fluid after REE mineral saturation,
388 the profiles also display weak HREE enrichment. The absolute concentrations of the
389 individual REE, however, are considerably higher for the Capitan Mountains samples
390 than for Baoshan, e.g., ~75-335 ppm versus 0.72 ppm for La and ~1.2-7.8 ppm versus
391 0.0048 ppm for Yb. This partly reflects the unusual, hypersaline nature of the Capitan
392 Mountains fluid, and the fact that it deposited REE-minerals, whereas the Baoshan
393 fluid was clearly undersaturated in the REEs, which occur only in trace quantities in
394 minerals like scheelite. It may also, however, reflect the assumption that mineral-
395 aqueous fluid partition coefficients are equivalent to mineral-melt partition
396 coefficients. In view of the above, we therefore conclude that the relative REE
397 concentrations predicted by the modeling (but not their absolute values) are reliable.

398 We used the REE content of the fluid determined above to extract the LSM
399 parameters for scheelite at its crystallization temperature, assuming that the REE
400 content of the fluid did not change significantly until the end of prograde skarn
401 formation. This temperature was assumed to be 427 °C (700 K), which is within the
402 range of temperature that has been determined for scheelite-bearing late prograde or
403 early retrograde garnet-pyroxene skarns (e.g., [Singoyi and Zaw, 2001](#); [Lu et al., 2003](#);

404 [Timón et al., 2009](#); [Soloviev, 2011](#)). In as much as at least three REEs were sufficient
 405 to obtain a unique solution for [Equation 5](#), we used those in greatest abundance for
 406 this purpose, i.e., La, Ce, Pr, Nd, Sm, Gd, and Tb. We calculated the REE partition
 407 coefficients for the average Scheelite II composition by fitting the Scheelite II-
 408 Baoshan fluid REE concentration ratios iteratively to [Equation 5](#) ([Fig. 12B](#);
 409 [Supplementary Data Table A3](#)). This produced values for D_0 , r_0 and E of 660 ($T=700$
 410 K), 1.072 Å, and 4,565 kbar, respectively. In order to assess the reliability of the
 411 values for r_0 and E , we used the empirical equations of [Hazen and Finger \(1979\)](#) and
 412 [Blundy and Wood \(1994\)](#) to calculate these values independently. For r_0 , the equation
 413 is based on the metal-oxygen bond length, and for E , it is based on the correlation
 414 between Young's modulus and the charge/volume (Z/d^3) of the lattice site (Z : ionic
 415 charge; d : metal-oxygen bond length). The optimal radius, r_0 , for scheelite and
 416 powellite, is equal to the difference between the Ca-O bond length (2.457 Å for
 417 scheelite; 2.458 Å for powellite) and the radius of fourfold-coordinated O^{2-} ions
 418 (1.380 Å) ([Shannon, 1976](#); [Smyth and Bish, 1988](#); [Blundy and Wood, 2003](#)). The
 419 resulting r_0 values for scheelite ($CaWO_4$) and powellite ($CaMoO_4$) are 1.077 and
 420 1.078 Å, respectively, which are very close to the value for r_0 for Scheelite II of 1.072
 421 Å, which was determined above. The value of E was calculated to be between 2,273
 422 ($Z/d^3=0.2020$) and 2,275 ($Z/d^3=0.2023$) kbar. By contrast, our E value regressed for
 423 Scheelite II is 4,565 kbar. However, as shown by [Blundy and Wood \(2003\)](#), the true
 424 values of the Young's modulus can deviate from the estimated values by up to several
 425 thousands of kbar with Z/d^3 ratios of around 0.2. We therefore conclude that the
 426 regressed r_0 (1.072 Å) and E (4,565 kbar) values are consistent with those calculated
 427 empirically, and provide confidence that the mineral-fluid REE partition coefficients

determined for Scheelite II by regressing the clinopyroxene-predicted fluid composition are reliable for predicting relative concentrations of elements.

6.2.3. Estimating LSM parameters for Scheelite I and III

As discussed above, the uptake of the REE by the Mo-bearing scheelite was controlled by coupled substitutions involving eightfold- and fourfold-coordinated sites ([Substitution 4](#)). Owing to the rigidity of the fourfold WO₃ and MoO₃ lattice sites ([Smyth and Bish, 1988](#)), an element partitioning into the eightfold Ca-site will not be affected significantly by the concentration of Mo. Thus, the regressed r_0 (1.072 Å) for Scheelite II also can be used to model REE partitioning into Scheelite I and Scheelite III.

As noted earlier, values of E depend on temperature and pressure and thus, in principle, the E values for Scheelite I and particularly Scheelite III (retrograde skarn) should differ from those for Scheelite II. However, as the E value extracted for Scheelite II is similar to that for clinopyroxene (e.g., [Wood and Blundy, 1997](#); [Blundy and Wood, 2003](#)), we conclude that values of E for scheelite varied little with P and T during skarn formation ($P < 1$ GPa, $T < 1000$ K) and any potential variation can be ignored. Accordingly, the value of E (4,565 kbar) regressed for Scheelite II was assumed for Scheelite I and III.

The relative chondrite-normalized REE distributions for Scheelite I and III were predicted by a D_0 -normalized equation derived from the LSM equation ([Eq. 6](#)) as:

$$\log \frac{x_i D_0}{D_i} = \log x_i + \frac{4\pi N_A \log e}{R} \cdot \frac{E_M}{T} \left[\frac{r_0 (r_i - r_0)^2}{2} + \frac{(r_i - r_0)^3}{3} \right] \quad (7),$$

where x_i stands for the chondrite-normalized concentration of element i in scheelite.

6.2.4. Implications of the REE profiles for scheelite

451 The Baoshan tungsten deposit is typical of many tungsten skarns, in that it is
452 characterized by early Mo-enriched scheelite and late Mo-poor scheelite. This could
453 reflect a trend of decreasing temperature, as numerous studies have shown that during
454 scheelite formation, temperature decreases from near magmatic values (~625 to 450
455 °C) to between 300 and 200 °C (e.g., [Einaudi et al., 1981](#); [Newberry, 1998](#); [Singoyi
456 and Zaw, 2001](#); [Lu et al., 2003](#); [Meinert et al., 2005](#); [Timón et al., 2009](#); [Soloviev,
457 2011](#)). For example, at Kara, Tasmania, and Kensu, Kyrgyzstan, the early, relatively
458 Mo-enriched scheelite formed at temperatures up to 600 °C, whereas the late scheelite
459 formed at ~250 °C ([Zaw and Singoyi, 2000](#); [Singoyi and Zaw, 2001](#); [Soloviev, 2011](#)).
460 Accordingly, for the purpose of our calculations, we propose that in the Baoshan
461 skarns, the early Mo-rich Scheelite I precipitated at 900 K (627 °C), Scheelite II
462 precipitated at 700 K (see above) and the late Mo-rich Scheelite III precipitated at 500
463 K (227 °C). The relative REE distributions ($x_{REE}D_0/D_{REE}$) of the Baoshan
464 hydrothermal fluids in equilibrium with Scheelite I, II, and III were calculated from
465 the REE contents of these minerals and the corresponding assumed formation
466 temperatures using [Equation 7](#). They are illustrated in [Figure 13](#), from which it is
467 evident that the hydrothermal fluids responsible for precipitation of the three scheelite
468 types were very similar compositionally. This implies that they crystallized from the
469 same magmatic fluid, except perhaps Scheelite III, which may have crystallized from
470 a modified meteoric fluid and acquired a magmatic signature by remobilizing
471 Scheelite II.

472 A feature of the fluid during the precipitation of Scheelite I is that it was depleted
473 in MREEs and HREEs relative to Scheelite II ([Fig. 13a and b](#)). We speculate that this
474 was the result of reaction of the fluid with limestone to form the garnet-clinopyroxene
475 skarn, and the preferential incorporation in the garnet of the MREE and HREE (e.g.,

476 [Smith et al., 2004](#); [Gaspar et al., 2008](#)). Another related feature already referred to, is
477 that the earliest scheelite (Scheelite I) was the most enriched in Mo, and the Mo
478 content decreased progressively from Scheelite II to Scheelite III. As discussed
479 previously, the formation of early Mo-enriched Scheelite I corresponds to a high
480 $\text{Mo}^{6+}(\text{Mo}^{5+})/\text{Mo}^{4+}$ ratio in the fluid and thus oxidizing conditions, whereas the lower
481 Mo content of the later scheelite types likely reflects lower values of this ratio and
482 more reducing conditions ([Hsu and Galli, 1973](#); [Hsu, 1977](#); [Rempel et al., 2009](#)). This
483 may parallel the zonation of the skarn from garnet (Fe^{3+}) near the granite to pyroxene
484 (Fe^{2+}) distal from it, which also records a trend from oxidizing to reducing conditions
485 ([Meinert et al., 2005](#)). However, all that is evident from the textural relationships is
486 that Scheelite I preceded pyroxene crystallization (Scheelite I is mantled by pyroxene)
487 and Scheelite II occurs in interstices among pyroxene crystals. Scheelite is not
488 observed in contact with garnet. Nonetheless, it is reasonable to propose that the
489 decrease in Mo concentration from Scheelite Ib, to Scheelite Ia, and to Scheelite II
490 records a progressive decrease in oxygen fugacity with evolution of the prograde
491 hydrothermal system.

492 Although the changing redox conditions clearly played an important role in
493 controlling the scheelite chemistry, particularly in respect to Mo, it is possible that
494 other compositional parameters also played a role. Indeed, it is noteworthy that
495 Scheelite II is accompanied by fluorite, which suggests that HF and F^- activity was
496 higher than in the preceding stage. As the Nb and Ta contents of Scheelite II are
497 higher than those of the other two scheelite types (Table 1), and as Nb and Ta have
498 been shown experimentally to reach their highest concentrations in hydrothermal
499 fluids as hydroxy-fluoride complexes (Timofeev et al., 2015, 2017), it seems highly

likely that an elevated HF activity was partly responsible for the high Nb and Ta contents of Scheelite II.

Although the REE composition interpreted for the fluid responsible for the deposition of Scheelite III is very similar to that interpreted for Scheelite I and Scheelite II, the distribution of the REE in Scheelite III differs from those in Scheelite I and II in one important respect. The Eu anomaly for Scheelite III is positive, whereas those for Scheelite I and II are weakly negative. A possible explanation for this lies in the observation that the difference between the radii of Eu^{2+} (1.250 Å) and Ca^{2+} (1.120 Å) in eightfold co-ordination is greater than that between Eu^{3+} (1.066 Å) and La^{3+} (1.072 Å) ([Shannon, 1976](#)). Based on experimental measurements and theoretical estimates of the proportions of divalent and trivalent cations in the fourfold site of clinopyroxene ([Blundy and Wood, 1994](#)), we speculate that the scheelite-fluid partition coefficient of Eu^{3+} is significantly greater than that of Eu^{2+} , which is consistent with the findings of [Nassau and Loiacono \(1963\)](#) and [Brugger et al. \(2000\)](#). Consequently, if conditions are very oxidizing, the $\text{Eu}^{3+}/\text{Eu}^{2+}$ ratio of the fluid will be unusually high and Eu will tend to incorporate preferentially in scheelite, producing a positive Eu anomaly. Although the high Mo content of Scheelite I attests to a relatively high oxygen fugacity and the lower Mo content of Scheelite II to more reducing conditions, we infer that conditions were most oxidizing during the retrograde event responsible for Scheelite III. We suggest that this was the case due to the influx of a relatively low temperature external fluid of meteoric origin, and propose that this fluid locally remobilized Scheelite II to form Scheelite III. Owing to the high oxygen fugacity, Eu^{3+} was therefore concentrated preferentially in Scheelite III, and due to the low temperature, Mo precipitated as molybdenite ([Williams-Jones and Migdisov, 2014](#)).

525 7. Conclusions

526 Scheelite in the Baoshan skarns evolved from an early Mo-rich prograde variety
527 (Scheelite I) through a late prograde variety (Scheelite II) with an intermediate Mo
528 content to a Mo-poor retrograde variety (Scheelite III). Incorporation of REEs into
529 scheelite was controlled by a fourfold-site compensating substitution (i.e.,
530 $Ca^{2+} + Mo^{6+} = REE^{3+} + (1 - x)Mo^{5+} + xNb^{5+}$ ($0 \leq x \leq 1$)). The concentrations of
531 the REEs in the fluid interpreted to have been responsible for prograde skarn
532 formation were estimated using the lattice strain model and the corresponding REE
533 concentrations in the pyroxene. The fluid was shown to be strongly enriched in the
534 LREE, depleted in the MREE and modestly enriched in the HREE. These data were
535 used to extract lattice strain parameters for Scheelite II (r_0 and E), on the assumption
536 that the magmatic fluid in equilibrium with the pyroxene also crystallized Scheelite II.
537 The same values of the lattice strain parameters were used for Scheelite I and III.
538 Application of the lattice strain model showed that relative to D_0 , which could not be
539 estimated reliably, the distribution of the REEs in the fluid was similar during all
540 stages of scheelite deposition, but evolved from strong enrichment in the LREE and
541 strong depletion in the MREE during Scheelite I deposition to weaker enrichment in
542 the LREE and less depletion in the MREE during crystallization of Scheelite III. The
543 Eu^{3+}/Eu^{2+} ratio evolved from relatively low in Scheelite I and II to high in Scheelite
544 III. The model that best fits the data is one in which conditions were initially
545 oxidizing, leading to strong incorporation of Mo in Scheelite I, became more reducing
546 with less incorporation of Mo in Scheelite II, and during retrograde skarn formation II
547 became oxidizing due to an influx of meteoric waters, which mobilized Scheelite II
548 and crystallized Scheelite III. This study provides a clear demonstration of the

549 potential utility of scheelite REE chemistry for quantitatively interpreting
550 hydrothermal processes.

551 **Acknowledgments**

552 We thank Prof. Jianfeng Gao, Dr. Tao Luo, and Dr. Yangzhou Tian for
553 laboratory assistance and discussion of the data. Mr. Shaoyi Wang and Mr. Xiang
554 Ouyang are thanked for their assistance in the field. Prof. Julian Pearce, Dr. Daniel
555 Harlov, and Dr. Xingxing Kuang, all provided very helpful discussions of our initial
556 ideas. This research was supported financially by the Special Fund for Public Welfare
557 Professions from Ministry of Land and Resources of People's Republic of China
558 (201411050) and a research grant from the Research Grant Council of Hong Kong.

559 **References**

- 560 Banks, D.A., Yardley, B.W.D., Campbell, A.R., Jarvis, K.E., 1994. REE composition
561 of an aqueous magmatic fluid: a fluid inclusion study from the Capitan Pluton,
562 New Mexico, USA. *Chemical Geology*, 113(3): 259-272.
- 563 Bau, M., 1991. Rare-earth element mobility during hydrothermal and metamorphic
564 fluid-rock interaction and the significance of the oxidation state of europium.
565 *Chemical Geology*, 93(3): 219-230.
- 566 Bau, M., 1996. Controls on the fractionation of isovalent trace elements in magmatic
567 and aqueous systems: evidence from Y/Ho, Zr/Hf, and lanthanide tetrad effect.
568 *Contributions to Mineralogy and Petrology*, 123(3): 323-333.
- 569 Blundy, J., Wood, B., 1994. Prediction of crystal melt partition coefficients from
570 elastic moduli. *Nature*, 372: 452-454.
- 571 Blundy, J., Wood, B., 2003. Partitioning of trace elements between crystals and melts.
572 *Earth and Planetary Science Letters*, 210(3): 383-397.

573 Brice, J.C., 1975. Some thermodynamic aspects of the growth of strained crystals.
 574 Journal of Crystal Growth, 28(2): 249-253.

575 Brugger, J., Etschmann, B., Pownceby, M., Liu, W.H., Grundler, P., Brewe, D., 2008.
 576 Oxidation state of europium in scheelite: Tracking fluid-rock interaction in
 577 gold deposits. Chemical Geology, 257(1-2): 26-33.

578 Brugger, J., Giere, R., Grobety, B., Uspensky, E., 1998. Scheelite-powellite and
 579 paraniite-(Y) from the Fe-Mn deposit at Fianel, Eastern Swiss Alps. American
 580 Mineralogist, 83: 1100-1110.

581 Brugger, J., Lahaye, Y., Costa, S., Lambert, D., Bateman, R., 2000. Inhomogeneous
 582 distribution of REE in scheelite and dynamics of Archaean hydrothermal
 583 systems (Mt. Charlotte and Drysdale gold deposits, Western Australia).
 584 Contributions to Mineralogy and Petrology, 139(3): 251-264.

585 Brugger, J., Maas, R., Lahaye, Y., McRae, C., Ghaderi, M., Costa, S., Lambert, D.,
 586 Bateman, R., Prince, K., 2002. Origins of Nd-Sr-Pb isotopic variations in
 587 single scheelite grains from Archaean gold deposits, Western Australia.
 588 Chemical Geology, 182(2-4): 203-225.

589 Burt, D.M., 1989. Compositional and phase relations among rare earth element
 590 minerals. Reviews of Mineralogy, 21: 260-307.

591 Einaudi, M.T., Meinert, L.D., Newberry, R.J., 1981. Skarn deposits. Economic
 592 Geology, 75: 317-391.

593 Gaspar, M., Knaack, C., Meinert, L.D., Moretti, R., 2008. REE in skarn systems: A
 594 LA-ICP-MS study of garnets from the Crown Jewel gold deposit. Geochimica
 595 et Cosmochimica Acta, 72(1): 185-205.

- 596 Ghaderi, M., Palin, J.M., Campbell, I.H., Sylvester, P.J., 1999. Rare earth element
597 systematics in scheelite from hydrothermal gold deposits in the Kalgoorlie-
598 Norseman region, Western Australia. *Economic Geology*, 94(3): 423-437.
- 599 Guo, C., 2010. Study on mineralization-related Mesozoic granitoids in Chongyi-
600 Shangyou Counties, South Jiangxi, and comparison to corresponding
601 granitoids in the Nanling region, South China, Chinese Academy of
602 Geological Sciences, Chinese Academy of Geological Sciences, 249 pp.
- 603 Guo, S., Chen, Y., Liu, C.-Z., Wang, J.-G., Su, B., Gao, Y.-J., Wu, F.-Y., Sein, K.,
604 Yang, Y.-H., Mao, Q., 2016. Scheelite and coexisting F-rich zoned garnet,
605 vesuvianite, fluorite, and apatite in calc-silicate rocks from the Mogok
606 metamorphic belt, Myanmar: Implications for metasomatism in marble and
607 the role of halogens in W mobilization and mineralization. *Journal of Asian*
608 *Earth Sciences*, 117: 82-106.
- 609 Hanson, G.N., 1980. Rare earth elements in petrogenetic studies of igneous systems.
610 *Annual Review of Earth and Planetary Sciences*, 8(1): 371-406.
- 611 Hazen, R.M., Finger, L.W., 1979. Bulk modulus—volume relationship for
612 cation anion polyhedra. *Journal of Geophysical Research: Solid Earth*,
613 84(B12): 6723-6728.
- 614 Hill, E., Blundy, J., Wood, B., 2011. Clinopyroxene-melt trace element partitioning
615 and the development of a predictive model for HFSE and Sc. *Contributions to*
616 *Mineralogy and Petrology*, 161(3): 423-438.
- 617 Hsu, L.C., 1977. Effects of oxygen and sulfur fugacities on the scheelite-tungstenite
618 and powellite-molybdenite stability relations. *Economic Geology*, 72(4): 664-
619 670.

620 Hsu, L.C., Galli, P.E., 1973. Origin of the scheelite-powellite series of minerals.
 621 Economic Geology, 68(5): 681-696.

622 Linnen, R.L., Samson, I.M., Williams-Jones, A.E., Chakhmouradian, A.R., 2014.
 623 Geochemistry of the rare-earth element, Nb, Ta, Hf, and Zr deposits. In:
 624 Turekian, H.D.H.K. (Ed.), Treatise on Geochemistry (Second Edition).
 625 Elsevier, Oxford, pp. 543-568.

626 Lipin, B.R., McKay, G.A., Boynton, W.V., 1989. Geochemistry and mineralogy of
 627 rare earth elements. Mineralogical Society of America Washington.

628 Liu, Y.S., Gao, S., Hu, Z.C., Gao, C.G., Zong, K.Q., Wang, D.B., 2010. Continental
 629 and oceanic crust recycling-induced melt-peridotite interactions in the Trans-
 630 North China Orogen: U-Pb dating, Hf isotopes and trace elements in zircons
 631 from mantle xenoliths. Journal of Petrology, 51(1-2): 537-571.

632 Liu, Y.S., Hu, Z.C., Gao, S., Gunther, D., Xu, J., Gao, C.G., Chen, H.H., 2008. In situ
 633 analysis of major and trace elements of anhydrous minerals by LA-ICP-MS
 634 without applying an internal standard. Chemical Geology, 257(1-2): 34-43.

635 Lu, H.-Z., Liu, Y., Wang, C., Xu, Y., Li, H., 2003. Mineralization and fluid inclusion
 636 study of the Shizhuyuan W-Sn-Bi-Mo-F skarn deposit, Hunan Province,
 637 China. Economic Geology, 98(5): 955-974.

638 Mao, J.W., Cheng, Y.B., Chen, M.H., Pirajno, F., 2013. Major types and time-space
 639 distribution of Mesozoic ore deposits in South China and their geodynamic
 640 settings. Mineralium Deposita, 48(3): 267-294.

641 McDonough, W.F., Sun, S.S., 1995. The composition of the Earth. Chemical
 642 Geology, 120(3): 223-253.

643 McIntire, W.L., 1963. Trace element partition coefficients—a review of theory and
 644 applications to geology. *Geochimica et Cosmochimica Acta*, 27(12): 1209-
 645 1264.

646 Meinert, L.D., Dipple, G.M., Nicolescu, S., 2005. World skarn deposits. *Economic*
 647 *Geology*, 100: 299-336.

648 Migdisov, A., Williams-Jones, A., Brugger, J., Caporuscio, F.A., 2016. Hydrothermal
 649 transport, deposition, and fractionation of the REE: Experimental data and
 650 thermodynamic calculations. *Chemical Geology*, 439: 13-42.

651 Migdisov, A.A., Williams-Jones, A.E., 2014. Hydrothermal transport and deposition
 652 of the rare earth elements by fluorine-bearing aqueous liquids. *Mineralium*
 653 *Deposita*, 49(8): 987-997.

654 Nassau, K., Loiacono, G.M., 1963. Calcium tungstate—III: Trivalent rare earth
 655 substitution. *Journal of Physics and Chemistry of Solids*, 24(12): 1503-1510.

656 Newberry, R.J., 1998. W-and Sn-skarn deposits: a 1998 status report. In: Lentz, D.R.
 657 (Ed.), *Mineralized Intrusion-Related Skarn Systems*. Mineralogical
 658 Association of Canada, Ottawa, pp. 289-335.

659 Olin, P.H., Wolff, J.A., 2010. Rare earth and high field strength element partitioning
 660 between iron-rich clinopyroxenes and felsic liquids. *Contributions to*
 661 *Mineralogy and Petrology*, 160(5): 761-775.

662 Pearson, R.G., 1963. Hard and Soft Acids and Bases. *Journal of the American*
 663 *Chemical Society*, 85(22): 3533-3539.

664 Poitrasson, F., Paquette, J.-L., Montel, J.-M., Pin, C., Duthou, J.-L., 1998. Importance
 665 of late-magmatic and hydrothermal fluids on the Sm–Nd isotope mineral
 666 systematics of hypersolvus granites. *Chemical Geology*, 146(3): 187-203.

- 667 Raimbault, L., Baumer, A., Dubru, M., Benkerrou, C., Croze, V., Zahm, A., 1993.
668 REE Fractionation between Scheelite and Apatite in Hydrothermal
669 Conditions. *American Mineralogist*, 78(11-12): 1275-1285.
- 670 Rempel, K.U., Williams-Jones, A.E., Migdisov, A.A., 2009. The partitioning of
671 molybdenum (VI) between aqueous liquid and vapour at temperatures up to
672 370 C. *Geochimica et Cosmochimica Acta*, 73(11): 3381-3392.
- 673 Shannon, R.D.t., 1976. Revised effective ionic radii and systematic studies of
674 interatomic distances in halides and chalcogenides. *Acta Crystallographica*
675 Section A: Crystal Physics, Diffraction, Theoretical and General
676 Crystallography, 32(5): 751-767.
- 677 Singoyi, B., Zaw, K., 2001. A petrological and fluid inclusion study of magnetite-
678 scheelite skarn mineralization at Kara, Northwestern Tasmania: implications
679 for ore genesis. *Chemical Geology*, 173(1-3): 239-253.
- 680 Smith, M.P., Henderson, P., Jeffries, T.E.R., Long, J., Williams, C.T., 2004. The rare
681 earth elements and uranium in garnets from the Beinn an Dubhaich Aureole,
682 Skye, Scotland, UK: constraints on processes in a dynamic hydrothermal
683 system. *Journal of Petrology*, 45(3): 457-484.
- 684 Smyth, J.R., Bish, D.L., 1988. Crystal structures and cation sites of the rock-forming
685 minerals. Allen & Unwin Boston.
- 686 Soloviev, S.G., 2011. Geology, mineralization, and fluid Inclusion characteristics of
687 the Kensu W-Mo skarn and Mo-W-Cu-Au alkalic porphyry deposit, Tien
688 Shan, Kyrgyzstan. *Economic Geology*, 106(2): 193-222.
- 689 Song, G.X., Qin, K.Z., Li, G.M., Evans, N.J., Chen, L., 2014. Scheelite elemental and
690 isotopic signatures: Implications for the genesis of skarn-type W-Mo deposits

691 in the Chizhou Area, Anhui Province, Eastern China. *American Mineralogist*,
692 99(2-3): 303-317.

693 Sun, K., Chen, B., 2017. Trace elements and Sr-Nd isotopes of scheelite: Implications
694 for the W-Cu-Mo polymetallic mineralization of the Shimensi deposit, South
695 China. *American Mineralogist*, 102(5): 1114-1128.

696 Timofeev, A., Migdisov, A.A., Williams-Jones, A., 2015. An experimental study of
697 the solubility and speciation of niobium in fluoride-bearing aqueous solutions
698 at elevated temperature. *Geochimica et Cosmochimica Acta*, 158: 103-111.

699 Timofeev, A., Migdisov, A.A., Williams-Jones, A., 2017. An experimental study of
700 the solubility and speciation of tantalum in fluoride-bearing aqueous solutions
701 at elevated temperature. *Geochimica et Cosmochimica Acta*, 197: 294-304.

702 Timón, S.M., Moro, M.C., Cembranos, M.L., 2009. Mineralogical and
703 physiochemical evolution of the Los Santos scheelite skarn, Salamanca, NW
704 Spain. *Economic Geology*, 104(7): 961-995.

705 Tyson, R.M., Hemphill, W.R., Theisen, A.F., 1988. Effect of the W: Mo ratio on the
706 shift of excitation and emission spectra in the scheelite-powellite series.
707 *American Mineralogist*, 73(9-10): 1145-1154.

708 Uspensky, E., Brugger, J., Gräser, S., 1998. REE geochemistry systematics of
709 scheelite from the Alps using luminescence spectroscopy: from global
710 regularities to local control. *Schweizerische Mineralogische und*
711 *Petrographische Mitteilungen*, 78(1): 31-54.

712 Williams-Jones, A.E., Migdisov, A.A., 2014. Experimental constraints on the
713 transport and deposition of metals in ore-forming hydrothermal systems.
714 *Economic Geology*, 18: 77-96.

715 Williams-Jones, A.E., Migdisov, A.A., Samson, I.M., 2012. Hydrothermal
 716 mobilisation of the rare earth elements—a tale of “ceria” and “yttria”.
 717 Elements, 8(5): 355-360.

718 Wood, B.J., Blundy, J.D., 1997. A predictive model for rare earth element partitioning
 719 between clinopyroxene and anhydrous silicate melt. Contributions to
 720 Mineralogy and Petrology, 129(2-3): 166-181.

721 Zaw, K., Singoyi, B., 2000. Formation of magnetite-scheelite skarn mineralization at
 722 Kara, northwestern Tasmania: Evidence from mineral chemistry and stable
 723 isotopes. Economic Geology, 95(6): 1215-1230.

724 Zhao, W.W., Zhou, M.-F., 2015. In-situ LA-ICP-MS trace elemental analyses of
 725 magnetite: The Mesozoic Tengtie skarn Fe deposit in the Nanling Range,
 726 South China. Ore Geology Reviews, 65: 872-883.

727 Zhao, W.W., Zhou, M.-F., Li, Y.H.M., Zhao, Z., Gao, J.-F., 2017. Genetic types,
 728 mineralization styles, and geodynamic settings of Mesozoic tungsten deposits
 729 in South China. Journal of Asian Earth Sciences, 137: 109-140.

730 Zhou, X.M., Sun, T., Shen, W.Z., Shu, L.S., Niu, Y.L., 2006. Petrogenesis of
 731 Mesozoic granitoids and volcanic rocks in South China: A response to tectonic
 732 evolution. Episodes, 29(1): 26-33.

733

734

735

736

737

738

739

740 **Figure captions**

741 **Figure 1:** Geological sketch map of the Baoshan tungsten skarn deposit, Nanling,
742 South China, and a schematic cross section through the Western Ore Zone,
743 showing the location of samples used in this study.

744 **Figure 2:** **A:** A photograph of skarn located between altered granite and marble in the
745 underground working Level 410 of the Baoshan deposit. **B:** Skarn zoned from
746 garnet, pyroxene, wollastonite towards marble.

747 **Figure 3:** Paragenetic sequence of skarns in Baoshan deposit.

748 **Figure 4:** **A:** Prograde skarn assemblages of wollastonite and clinopyroxene under
749 crossed transmitted light. **B:** Mo-enriched scheelite and Mg-enriched
750 clinopyroxene enclosed in the altered Al-enriched garnet grain, under crossed
751 transmitted light. **C:** Mg-enriched clinopyroxene rimmed by Fe-enriched
752 clinopyroxene; andradite occurs in the pores of clinopyroxene, under crossed
753 transmitted light. **D:** Al-enriched garnet rimmed by Fe-enriched garnet
754 surrounded by clinopyroxene, under crossed transmitted light. **E:** Al-enriched
755 garnet replaced by Fe-enriched garnet, further altered by retrograde minerals,
756 under crossed transmitted light. **F:** the same region of Fig. 4E under plane
757 transmitted light; clinopyroxene and fluorite filling in the pores of the single
758 garnet grain. **G:** the retrograde chlorite in the pores of prograde garnet and
759 fluorite, under plane transmitted light. **H:** chalcopyrite and pyrrhotite in a quartz
760 vein cutting the prograde pyroxene skarn.

761 **Figure 5:** **A:** Anhedral scheelite coexisting with isotropic fluorite in pores within
762 pyroxene skarn. **B:** Granular fractured scheelite crystals surrounded by
763 clinopyroxene, and retrograde sulfides, such as molybdenite, that overprinted
764 these prograde minerals.

765 **Figure 6:** Back-scattered electron (BSE) and secondary electron (SE) images (A and
766 F) and cathodoluminescence (CL) images (B, C, D, E, and G) of scheelite. A, B,
767 C, D, and E: images of scheelite in Figure 2B, showing paragenetic relationship
768 among Scheelite I, Scheelite II, and Scheelite III. F, G: images of a scheelite
769 crystal from a pore in pyroxene skarn, showing Scheelite II overprinted by
770 Scheelite III.

771 **Figure 7:** Back-scattered electron (BSE) images of representative scheelite crystals
772 and chondrite-normalized REE profiles for the corresponding areas. Owing to the
773 extremely high contrast required to show zonation in the scheelite, the
774 surrounding minerals appear in black. A, B: BSE image of complexly zoned
775 scheelite (Sch I and Sch II), with REE profiles and major element compositions
776 of texturally defined regions. C, D: BSE image of zoned scheelite (Sch I and Sch
777 II), with REE profiles and major element compositions of core and rim. E, F:
778 BSE image of a single grain of extremely low-Mo scheelite (Sch III), with its
779 REE profile and major element composition. The diameter of the ablation crater
780 is ~25 μm . Concentrations were normalized to the chondrite values of
781 [McDonough and Sun \(1995\)](#).

782 **Figure 8:** Chondrite-normalized REE profiles of scheelite from the Baoshan tungsten
783 skarn. A: Scheelite I (Sch Ia and Sch Ib). B: Scheelite II (Sch II). C: Scheelite III
784 (Sch III). The dotted line shows the chondrite-normalized LA-ICP-MS detection
785 limits for each REE. Concentrations were normalized to the chondrite values of
786 [McDonough and Sun \(1995\)](#).

787 **Figure 9:** A plot of Mo in ppm versus total REEs (ΣREE) in ppm for Scheelite I, II
788 and III.

789 **Figure 10:** A: Plot of chondrite-normalized Eu concentrations (Eu_N) versus calculated
790 Eu^*_N values, where $Eu^*_N = (Sm_N \times Gd_N)^{1/2}$ for Scheelite I, II, and III. B: Eu_N/Eu^*_N
791 ratios versus Mo content for Scheelite I, II and III. Concentrations were
792 normalized to the chondrite values of [McDonough and Sun \(1995\)](#).

793 **Figure 11:** A: Plot of Na versus $\Sigma REE-Eu+Y$ of Scheelite I, II, and III. The dashed
794 line indicates the detection limits of LA-ICP-MS analyses for Na. B: Plots of
795 Nb+Ta versus $\Sigma REE-Eu+Y$ for Scheelite I, II, and III. The dashed line is the 1:1
796 correlation line assuming.

797 **Figure 12:** A: A schematic Onuma representation of the Lattice Strain Model (LSM)
798 showing the log (partition coefficient) versus the ionic radius for elements of the
799 same valence state and same coordination number. D_0 is the partition coefficient
800 for the optimal ionic radius r_0 , and E_M is the Young's modulus for the site. B:
801 Mineral-fluid partition coefficients for Bandolier Tuff Fe-rich clinopyroxene
802 reported by [Olin and Wolff \(2010\)](#), and for Scheelite II that were calculated (La,
803 Ce, Pr, Nd, Sm, Gd, and Tb; with error bars) and regressed using the composition
804 of the fluid in equilibrium with clinopyroxene (see text for further detail). Dashed
805 circles represent REEs (i.e., Dy, Ho, Er, Tm, and Lu) with analyses below
806 detection limits, which were not used for regression. C: Chondrite-normalized
807 REE concentrations of the fluid in equilibrium with Scheelite II calculated using
808 the partition coefficients illustrated in Fig.12B and in equilibrium with Fe-rich
809 clinopyroxene. Concentrations were normalized to the chondrite values of
810 [McDonough and Sun \(1995\)](#).

811 **Figure 13:** Predicted REE distributions in ore-forming fluids of different skarn stages
812 relative to. A: Scheelite I (Sch I). B: Scheelite II (Sch II). C: Scheelite III (Sch
813 III). The shaded region shows the ranges of data of Scheelite II. The letter *x* refers

814 to the chondrite-normalized REE concentrations in scheelite relative to D_0 .
815 Concentrations were normalized to the chondrite values of [McDonough and Sun](#)
816 [\(1995\)](#).
817

818 **Table 1:** Selected element concentrations (in ppm) of representative samples of
819 scheelite from Baoshan skarns.

820 **Supplementary Table A1:** EMP analyses (in wt % oxides) of scheelite from Baoshan
821 skarns.

822 **Supplementary Table A2:** Composition of the Baoshan and Bandolier Tuff Fe-rich
823 clinopyroxenes.

824 **Supplementary Table A3:** Data used in regression or for reference.

825 **Supplementary Table A4:** Major elemental compositions of garnet and
826 clinopyroxene from Baoshan skarns.

827

828

Table 1 Representative EMP and LA-ICP-MS analyses of scheelites from Baoshan skarns.

	First-stage scheelite (Sch I)												
	M7-Sopt 13	M4-Spot 55	M4-Spot 54	M2-Spot 131	M2-Spot 135	M4-Spot 52	M1-Spot 106	M6-Spot 22	M6-Spot 17	M6-Spot 13	M6-Spot 18	M1-Spot 113	M1-Spot 103
EMP analyses (in wt % oxides)													
MoO ₃	24.12	17.12	17.12	16.09	16.09	14.18	15.50	14.99	11.94	11.18	10.02	11.25	7.36
CaO	22.28	21.75	21.75	21.40	21.40	21.11	21.57	20.99	20.98	21.73	20.40	20.94	20.41
ZnO	-	0.01	0.01	-	-	-	-	0.01	-	-	-	-	-
MnO	0.02	-	-	0.02	0.02	-	-	0.03	-	0.01	0.01	0.03	0.01
WO ₃	54.91	62.01	62.01	63.34	63.34	65.36	64.13	66.28	68.91	66.79	69.73	70.47	72.76
SrO	-	-	-	-	-	-	-	-	-	-	-	-	-
PbO	-	-	-	-	-	-	-	-	-	-	-	-	-
FeO	0.01	-	-	-	-	0.02	0.01	0.16	0.06	0.10	0.02	0.06	-
Total	101.33	101.34	101.34	100.89	100.89	101.10	101.22	102.84	102.38	99.83	100.18	102.76	100.53
LA-ICP-MS analyses (in ppm)													
Na	-	50	-	32	33	-	-	-	-	-	-	-	-
Sr	30.6	57.4	67.2	58.9	60.3	47.0	64.7	71.5	55.1	57.8	53.2	44.7	33.5
Y	0.26	-	0.13	0.44	0.20	-	0.16	0.13	0.09	0.29	0.33	0.16	0.22
Zr	-	-	-	-	-	-	-	-	-	-	-	-	-
Nb	2.96	6.41	4.13	3.20	4.24	3.80	5.27	8.00	32.06	78.78	103.49	91.41	114.55
Mo	159159.1	126087.6	110506.5	100993.6	97943.7	92847.2	91548.6	89950.3	89355.3	79662.1	65032.7	64830.1	56393.2
La	6.40	8.21	4.33	7.80	11.33	6.46	11.24	19.56	24.42	51.53	44.64	54.43	52.05
Ce	6.79	10.48	5.37	9.01	12.57	8.06	13.62	24.50	37.24	70.96	67.64	83.13	70.12
Pr	0.54	0.67	0.37	0.76	0.94	0.49	0.92	1.87	2.93	5.01	5.17	6.33	5.35
Nd	1.2	1.4	1.4	1.8	2.1	0.7	1.3	2.7	4.8	7.2	8.1	12.2	8.4
Sm	-	-	-	0.2	-	-	0.2	-	-	0.2	0.7	0.7	0.2
Eu	-	-	-	0.05	-	0.04	-	0.05	-	0.04	-	0.07	-
Gd	-	-	-	-	-	-	-	-	0.2	0.3	-	0.6	-
Tb	-	-	-	-	-	-	-	-	-	0.02	0.05	-	0.03
Dy	-	-	0.16	0.11	-	0.10	-	0.09	0.18	-	-	0.17	-
Ho	-	-	-	-	-	-	-	0.03	0.08	-	-	-	-
Er	-	-	-	0.07	-	-	-	-	0.07	0.05	0.27	-	-
Tm	-	-	-	-	-	-	-	-	-	-	-	-	-
Yb	-	0.2	-	-	-	-	-	-	-	-	-	-	-
Lu	-	-	0.02	-	-	0.02	-	-	-	-	0.06	-	-
Hf	-	-	-	-	-	-	-	-	-	-	-	-	-
Ta	-	0.08	0.08	0.09	0.09	0.07	0.06	0.02	0.06	0.06	0.12	0.16	0.15
Pb	7.39	4.42	3.43	4.10	3.63	3.92	4.18	3.93	2.84	3.18	7.94	2.09	3.40
ΣREE	14.94	20.99	11.63	19.85	26.94	15.89	27.29	48.82	69.93	135.41	126.72	157.57	136.22

Continue in next page

Table 1 Continues

	Second-stage scheelite (Sch II)										Third-stage scheelite (Sch III)		
	M2-Spot 124	M6-Spot 25	M2-Spot 125	M2-Spot 126	M6-Spot 23	M5-Spot 28	M1-Spot 107	M3-Spot 60	M1-Spot 97	M1-Spot 104	M3-Spot 57	M3-Spot 66	M3-Spot 58
EMP analyses (in wt % oxides)													
MoO ₃	1.65	1.24	1.65	1.41	1.19	1.32	1.29	1.19	1.07	0.78	-	0.02	0.06
CaO	19.70	19.00	19.70	19.64	19.46	19.77	19.84	19.73	19.62	19.47	19.64	19.52	19.80
ZnO	-	-	-	-	-	-	-	-	-	0.01	0.01	-	-
MnO	0.03	0.01	0.03	-	-	-	-	-	0.01	0.02	-	0.03	0.02
WO ₃	79.05	79.22	79.05	79.02	80.33	79.65	80.09	80.31	80.22	80.62	82.17	82.17	81.19
SrO	-	-	-	-	-	-	-	-	-	-	-	-	-
PbO	-	-	-	-	-	-	-	-	-	-	0.01	-	-
FeO	0.23	0.04	0.23	0.06	0.02	0.06	0.16	0.04	0.16	0.02	0.14	0.22	0.23
Total	100.67	99.80	100.67	100.52	101.02	100.82	101.40	101.28	101.33	100.93	101.98	102.46	101.33
LA-ICP-MS analyses (in ppm)													
Na	-	20	23	27	-	-	-	-	24	-	-	-	22
Sr	24.2	16.9	22.6	19.3	18.6	19.6	25.4	22.1	16.0	15.6	52.2	53.2	49.5
Y	0.80	0.61	0.36	0.84	0.71	3.87	1.72	1.33	2.80	3.16	2.22	10.74	3.02
Zr	-	-	-	-	-	-	-	-	-	-	-	-	-
Nb	100.54	81.82	122.02	108.31	78.97	75.44	65.24	72.14	61.43	97.34	53.94	79.27	79.48
Mo	9862.2	9795.9	9714.0	9089.6	8852.7	8411.1	8208.8	7676.2	7399.9	6925.4	53.5	89.2	87.3
La	48.02	43.05	47.76	39.49	36.23	28.93	25.38	30.85	35.83	29.67	13.05	72.08	35.28
Ce	96.26	90.12	106.36	101.33	83.80	78.67	56.66	69.24	89.17	93.37	13.76	139.13	59.77
Pr	11.13	8.70	11.68	11.13	10.82	12.52	6.54	7.98	10.91	11.46	1.79	16.20	8.10
Nd	31.5	19.7	29.1	27.8	29.6	39.4	19.5	25.1	28.1	34.3	5.8	55.2	30.3
Sm	2.2	1.7	1.7	1.2	3.4	5.0	2.5	5.1	4.3	4.8	1.5	13.7	9.3
Eu	0.20	0.23	0.22	0.14	0.20	0.38	0.51	0.50	0.50	0.44	5.37	11.82	6.66
Gd	0.6	0.5	0.4	1.0	0.9	2.7	1.7	1.6	2.0	2.1	0.5	6.1	3.1
Tb	0.11	0.06	0.02	0.06	0.17	0.24	0.17	0.14	0.18	0.24	0.05	0.75	0.34
Dy	-	0.16	-	0.16	0.26	0.68	0.82	0.35	1.17	0.78	0.24	3.70	1.46
Ho	-	-	0.02	-	0.03	0.17	0.04	0.02	0.07	0.12	0.02	0.38	0.11
Er	0.12	-	-	-	0.11	0.21	0.13	0.13	0.28	0.13	0.18	0.78	0.42
Tm	-	-	-	-	-	0.02	0.02	-	0.04	-	-	0.14	0.03
Yb	-	-	-	-	-	-	-	-	-	-	-	1.0	0.2
Lu	-	-	-	-	-	-	-	-	0.07	-	-	0.10	0.04
Hf	-	-	-	-	-	-	-	-	-	-	-	-	-
Ta	0.49	0.26	0.51	0.46	0.15	0.32	0.23	0.32	0.29	0.54	0.16	0.20	0.13
Pb	2.86	2.39	3.02	3.03	2.80	2.32	2.36	2.95	4.45	3.78	7.00	6.90	6.05
ΣREE	190.26	164.14	197.19	182.37	165.56	169.00	113.92	140.97	172.57	177.45	42.28	321.15	155.18

Note: "-": values that below the detection limits.

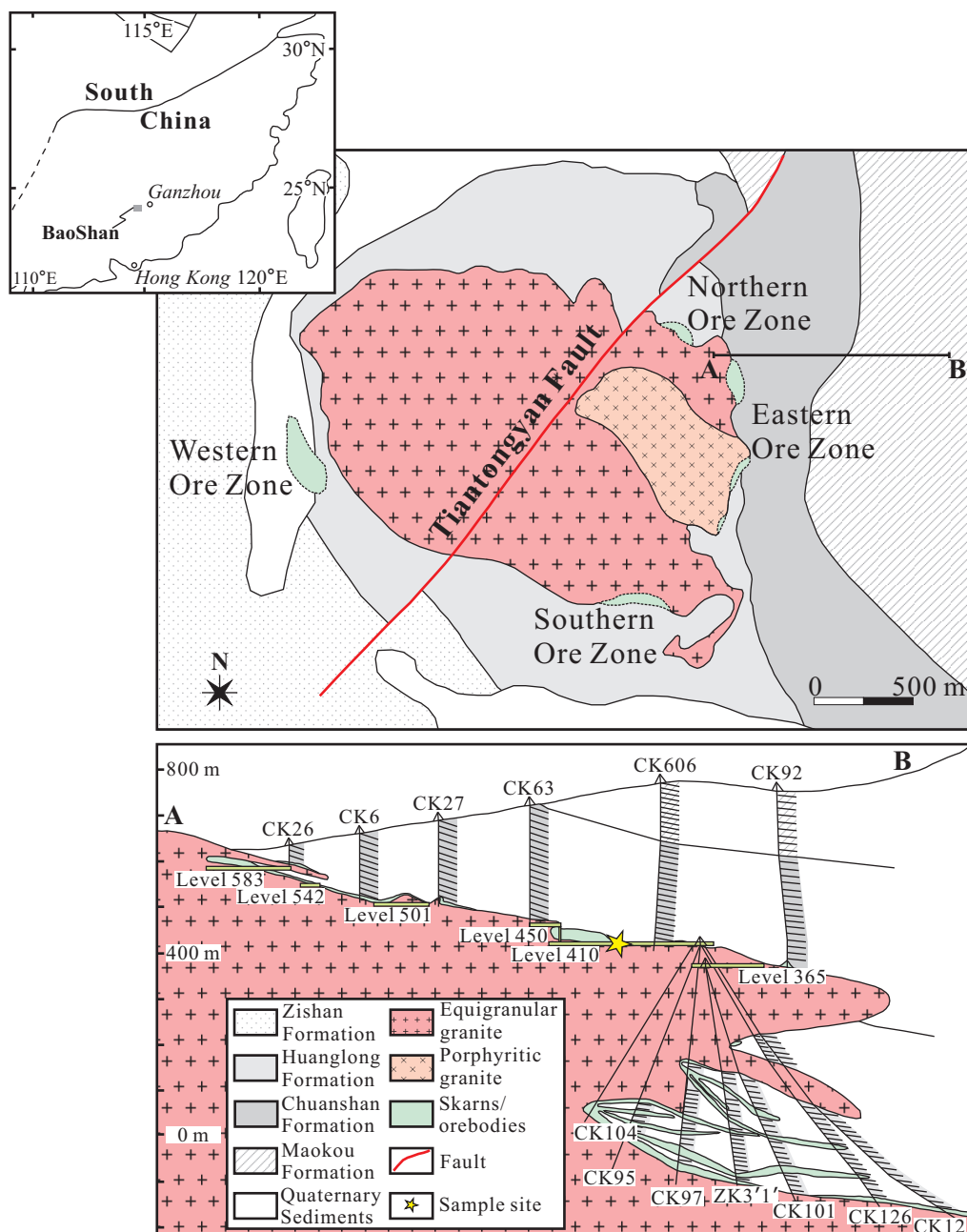


Figure 1

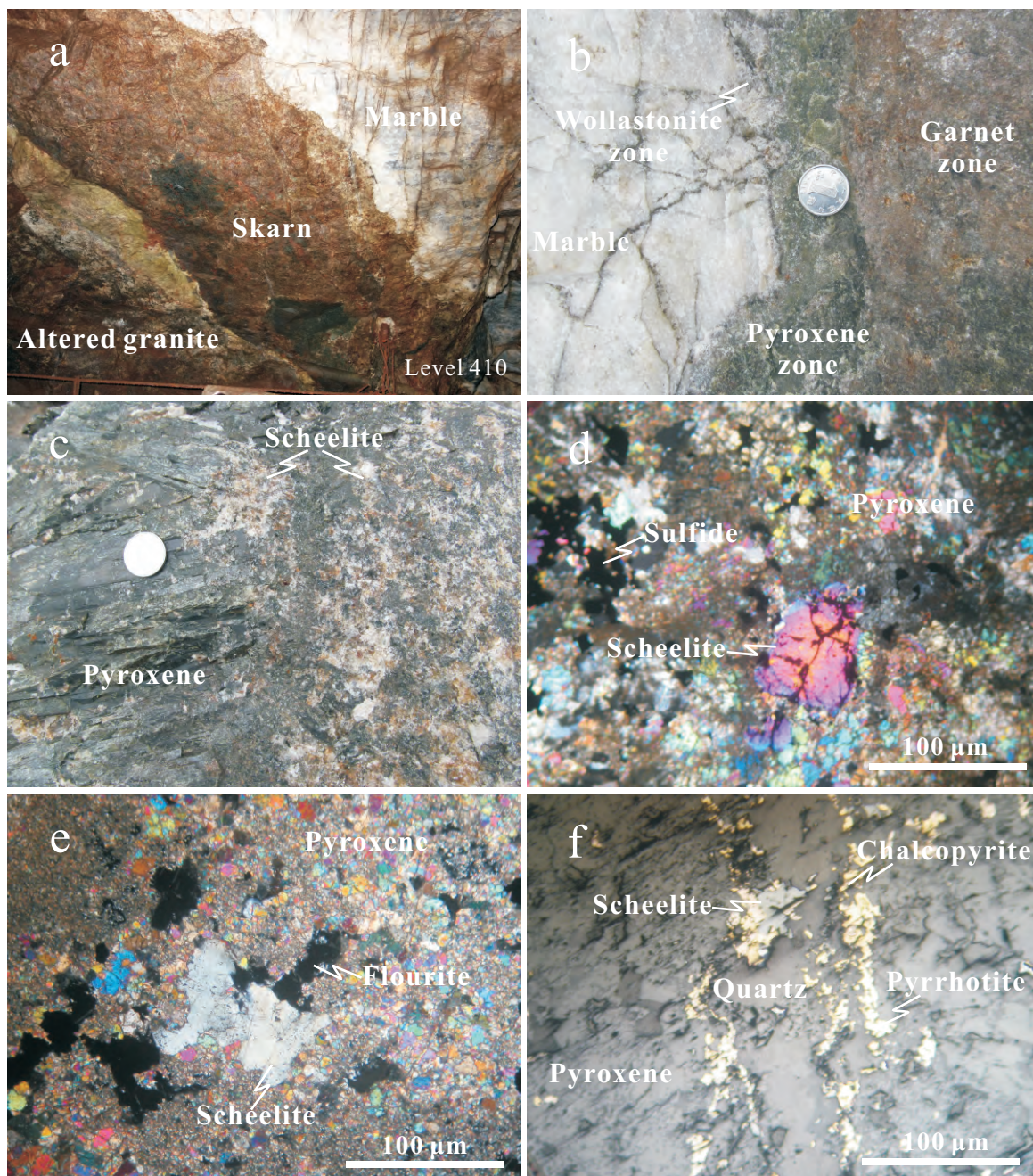


Figure 2

Zhao, W. W., M. F. Zhou, A. E. Williams-Jones, and Z. Zhao.
 "Constraints on the Uptake of Re by Scheelite in the Baoshan Tungsten Skarn Deposit, South China."
 Chemical Geology 477 (Jan 20 2018): 123-36. <http://dx.doi.org/10.1016/j.chemgeo.2017.12.020>.

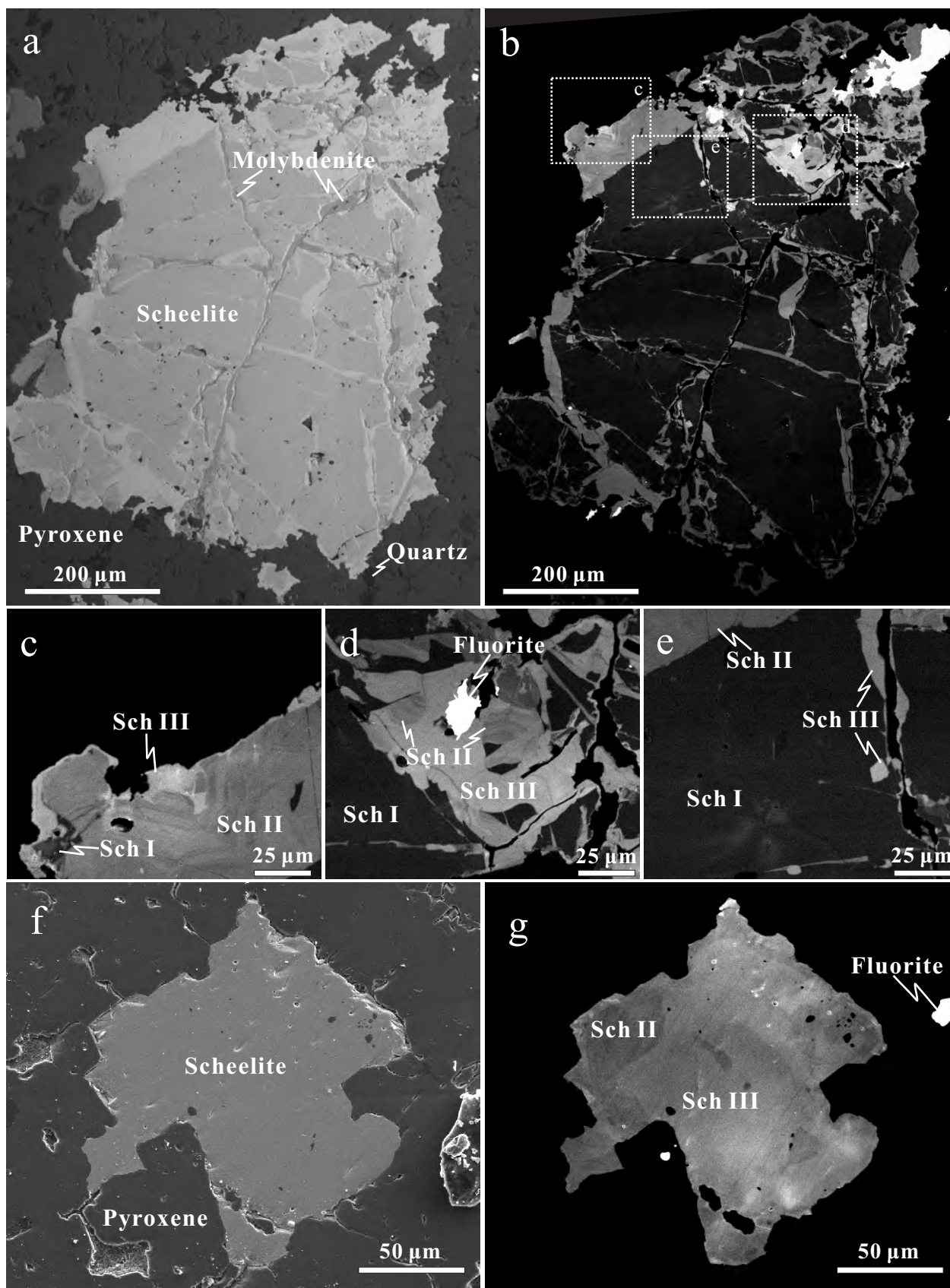


Figure 3

Zhao, W. W., M. F. Zhou, A. E. Williams-Jones, and Z. Zhao.
 "Constraints on the Uptake of Re by Scheelite in the Baoshan Tungsten Skarn Deposit, South China."
 Chemical Geology 477 (Jan 20 2018): 123-36. <http://dx.doi.org/10.1016/j.chemgeo.2017.12.020>.

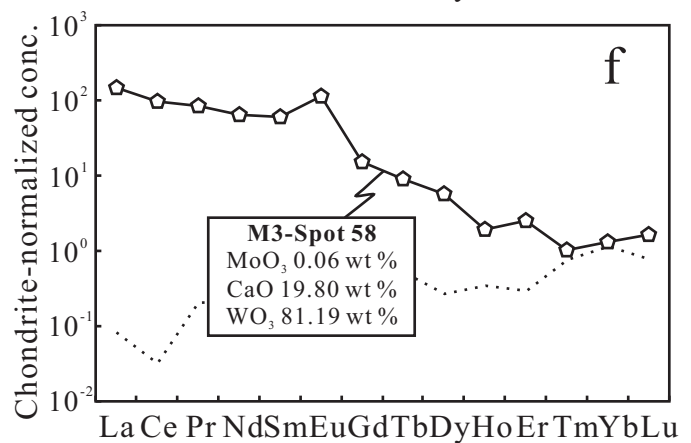
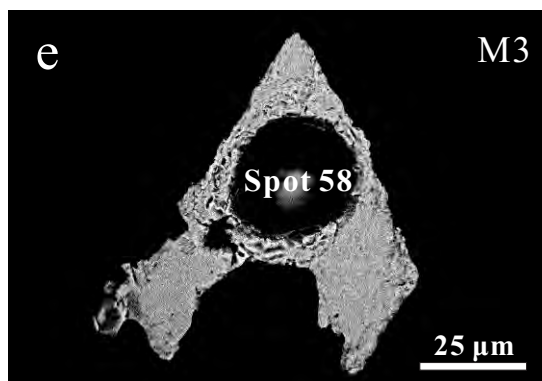
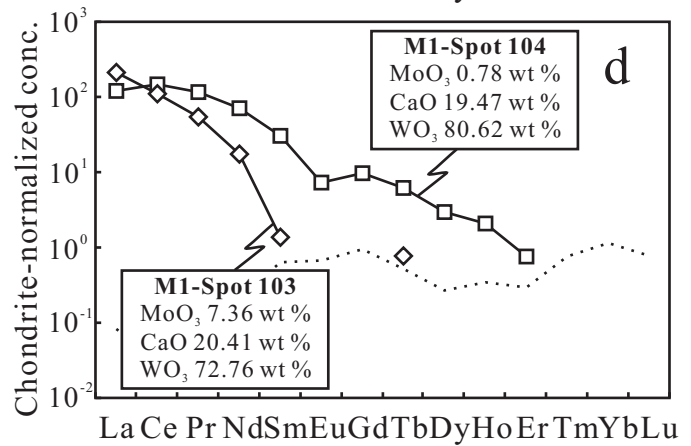
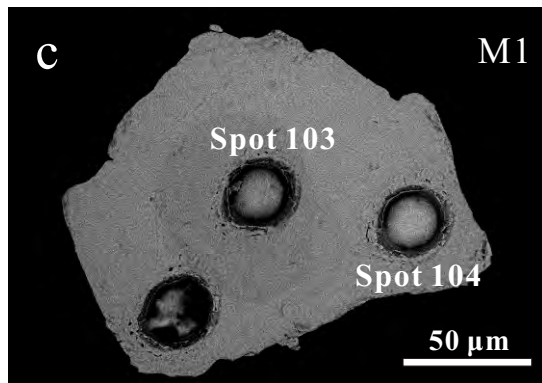
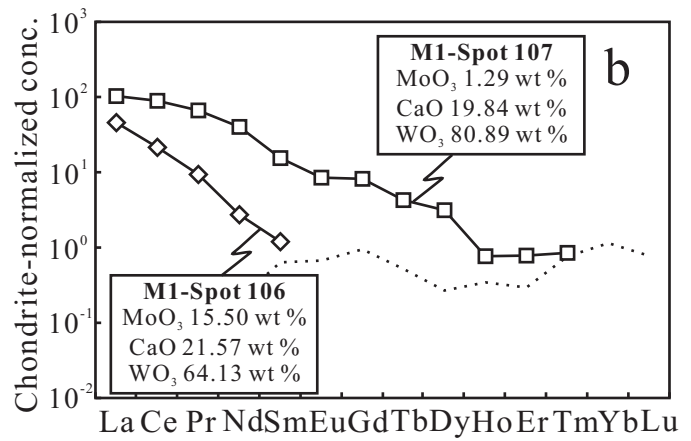
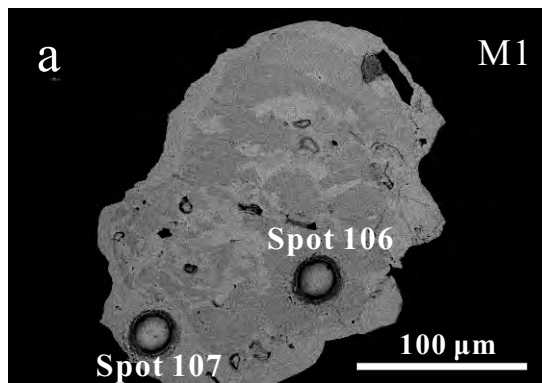


Figure 4

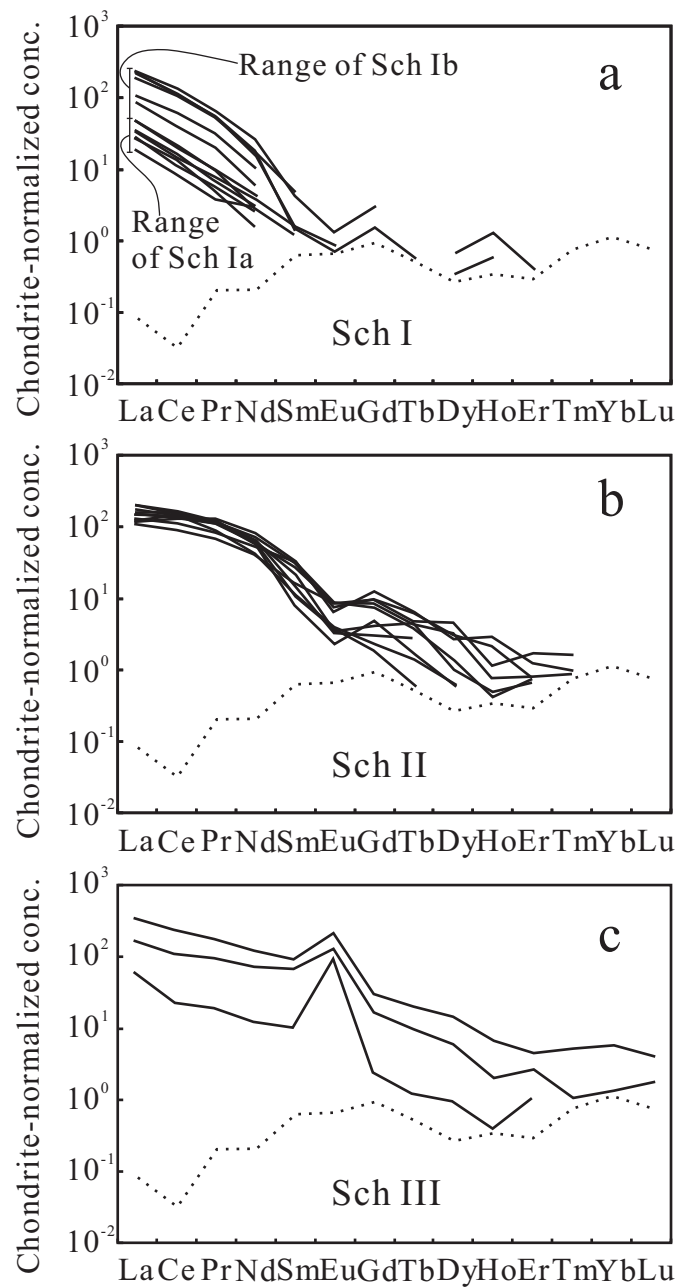


Figure 5

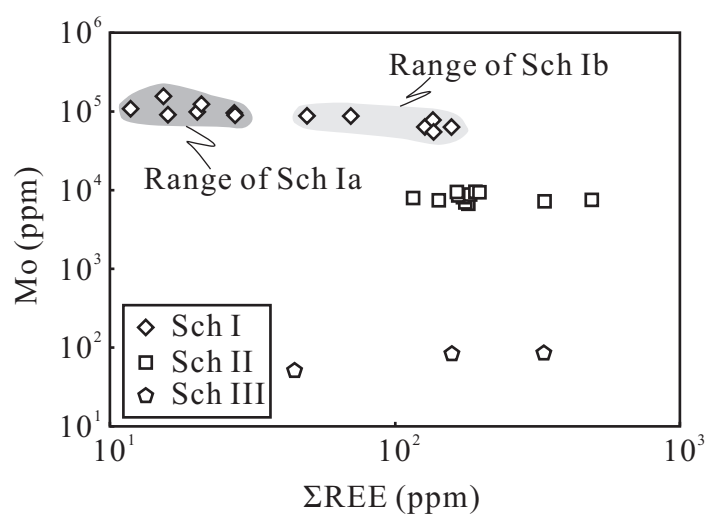


Figure 6

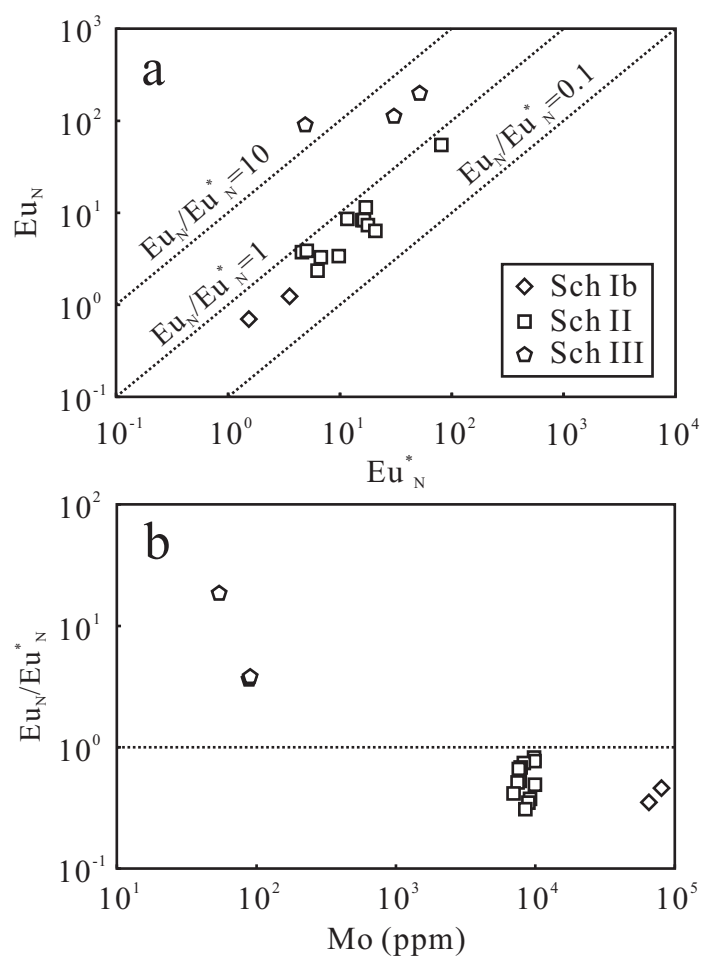


Figure 7

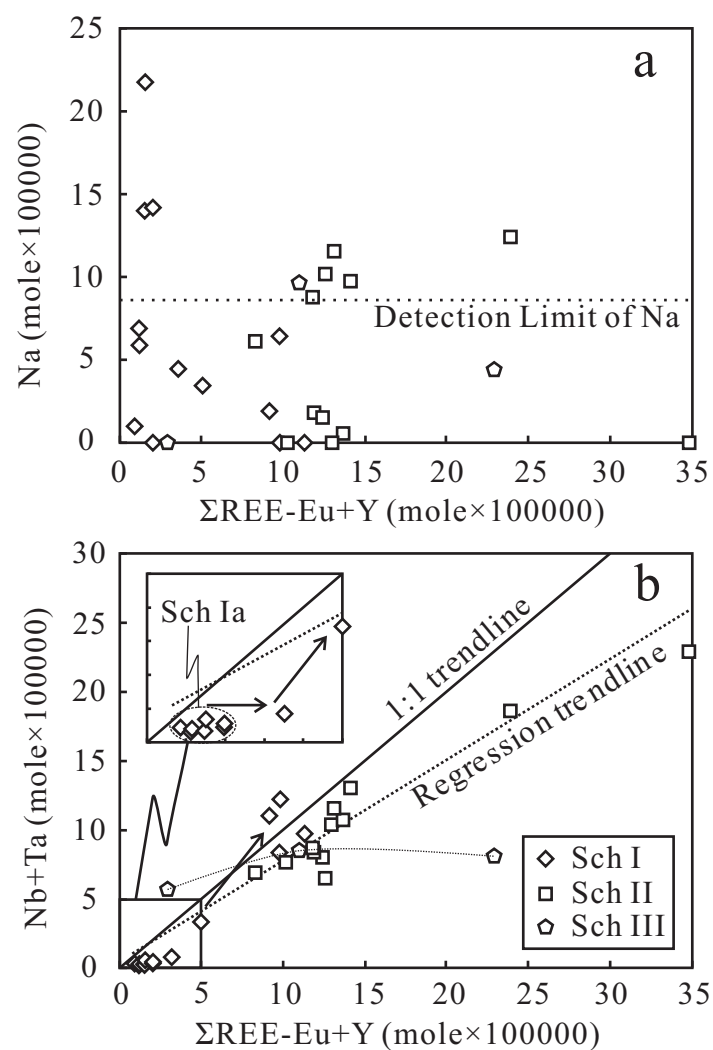


Figure 8

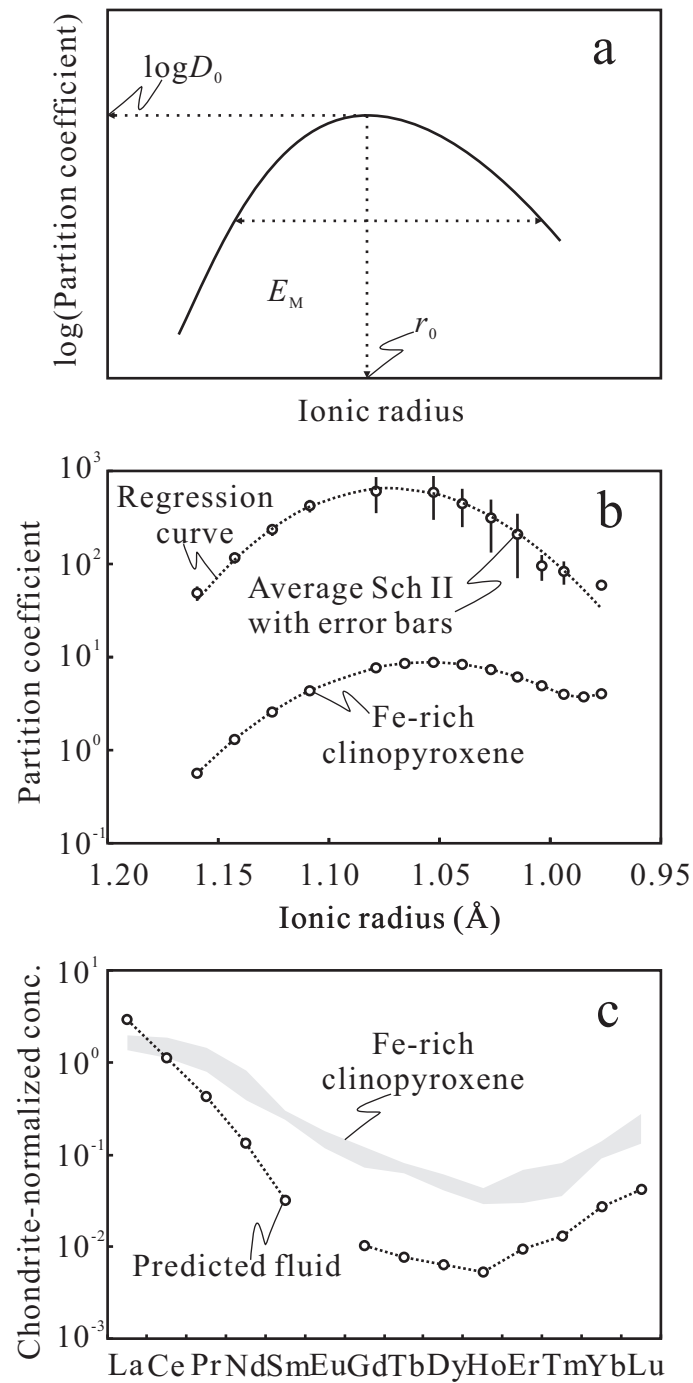


Figure 9

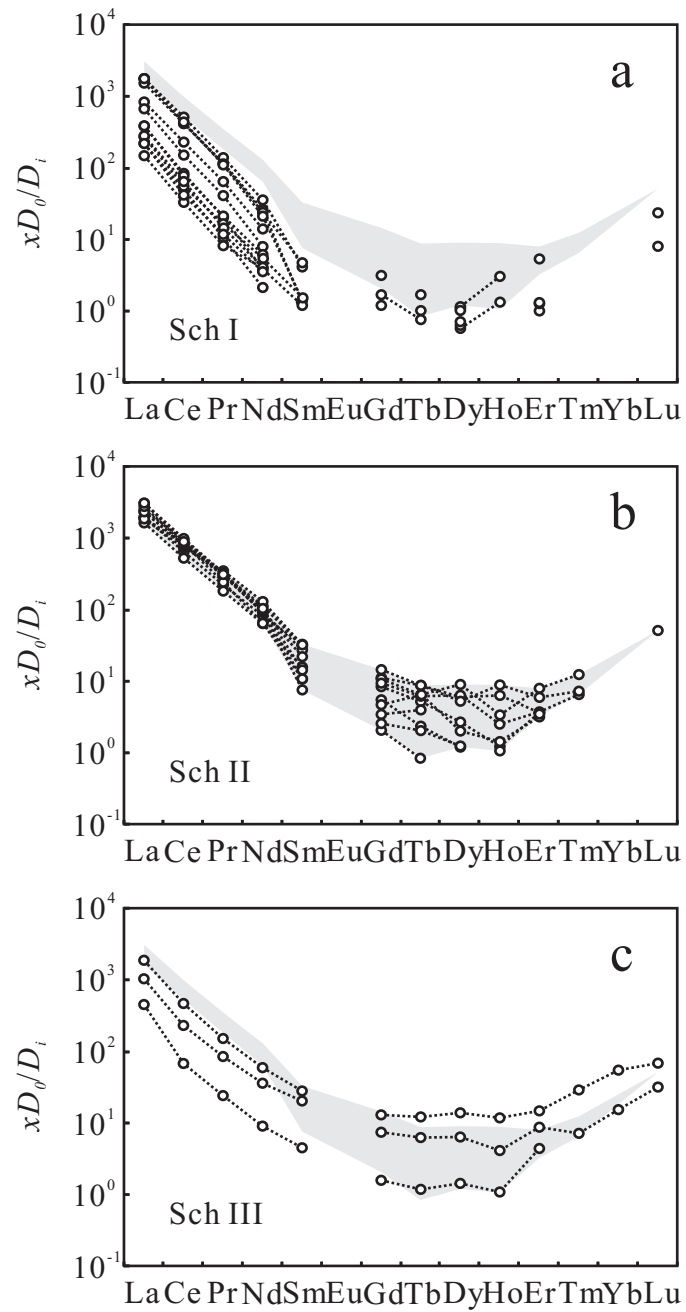


Figure 10